ANALYSIS OF HARBOR OSCILLATION WITH A BOUSSINESQ MODEL

A THESIS SUBMITTED TO THE GRADUATE DIVISION OF THE
UNIVERSITY OF HAWAI'I IN PARTIAL FULFILLMENT
OF THE REQUIREMENTS FOR THE DEGREE OF

MASTER OF SCIENCE

IN

OCEAN ENGINEERING

AUGUST 2003

By

Yann M.J. Douyère

Thesis Committee:

Kwok Fai Cheung, Chairperson
Hans-Jürgen Krock
Mark A. Merrifield

ACKNOWLEDGMENTS

I would like to express my appreciation to all who contributed to this thesis and in particular to Dr. Kwok Fai Cheung, whose thorough engineering knowledge and valuable academic advice have contributed to the realization of this project. Many thanks also go to the committee members Dr. Hans-Jürgen Krock and Dr. Mark A. Merrifield for their support and advice throughout. I would also like to thank Dr. Philip L.-F. Liu and Dr. Patrick Lynett for providing the Boussinesq code and supporting its application and Dr. Zeki Demirbilek for providing the bathymetry data for this study. Thanks are also due to Mr. Wei Yong, Mr. Yang Jinghai, and Dr. David A. Smith for their valuable input on the project. Many thanks go to Ms. Edith Katada for her time and expertise in the departmental procedures. The spirit of this Ocean and Resources Engineering department is an inspiration. Here we learn the ability to cherish our ocean most of all. Thank you all; I could not have completed this report without your help. I am glad we have become friends.

Financial support in the form of a research assistantship was provided through projects sponsored by NASA Office of Earth Science under grant no. NAG5-8748 and ONR Division of Ship Science and Technology under grant no. N00014-02-01-0903.

ABSTRACT

Seiches or long-wave oscillations in harbors are normally the result of nonlinear interactions within groups of narrow-banded wind waves and swell. These oscillations may cause excessive vessel motions and disrupt loading and unloading operations at port facilities. Accurate prediction of harbor oscillation patterns is therefore an important aspect in harbor design. Most previous studies have used linear models to predict these nonlinear oscillation behaviors. This study uses an extended Boussinesq model that is applicable from deep to shallow water and takes into account the generation mechanism of these oscillations along with their interaction with the wind waves or swell. The finite-difference model utilizes a predictor-corrector scheme to march the solution forward in time. It has a moving boundary algorithm to account for wave swashing, thereby allowing the correct boundary condition to be imposed at shorelines. The model is applied to examine the natural oscillation modes at Barbers Point Harbor and Kahului Harbor located on the West and North shores of Oahu and Maui respectively. The computed responses at each harbor are compared with previous linear model results and data gathered from pressure sensors. The analysis shows that harbor oscillation is primarily excited by infragravity waves, which can be simulated by a Boussinesq model.

TABLE OF CONTENTS

LIST OF FIGURES

LIST OF TABLES

1. INTRODUCTION

1.1 Harbor Oscillation

Wave climate plays an important role in harbor design and operations. Wu and Liu (1990) showed groups of narrow-banded wind waves and swell can induce long-period waves of 1 to 5 min through nonlinear interaction. If these long-period waves coincide with the natural periods of the harbor, resonance oscillations or seiching may occur. These oscillations are most damaging to moored vessels within the harbor basin, causing excessive vessel motion and delays of loading and unloading operations at port facilities. Excessive vessel motion may lead to the breaking of mooring lines and damage to fender systems, and in some situations, vessel collisions.

A basin can exhibit different modes of oscillation. The lowest mode of oscillation is commonly referred to as the Helmholtz or grave mode, in which the basin water surface rises and falls in unison with the oscillation of the channel water in and out of the harbor (Sorensen and Seelig, 1986). The higher modes are characterized by distinct nodes and antinodes in the oscillation pattern and are more critical to harbor operation. Figure 1-1 illustrates the natural oscillation modes in a rectangular basin. The number of nodes and antinodes is easily identifiable and characterizes the oscillation modes. For example, the fundamental mode contains one node and two antinodes. The oscillation pattern becomes more complicated for actual harbors with varying bathymetry.

1.2 Literature Review

Harbor oscillation has been studied extensively through field measurements, physical models, and numerical models. Each of these approaches has assumptions and limitations and does not necessarily produce the same results. These methods are usually used in combination to examine harbor oscillation problems. Prototype measurements are needed

for calibration or verification of numerical and physical models, which in turn can be used to evaluate different design layouts and produce a design that minimizes wave disturbance within the harbor.

1.2.1 Field Measurements and Physical Models

Field measurements are necessary in harbor planning or expansion. Important characteristics such as wave climate data, bottom friction, and current directions can be used to define test conditions in numerical or physical models. Field measurements have also been performed for existing harbors to provide better understanding of their oscillation characteristics and suggest design improvements. Okihiro et al. (1993) investigated the oscillations at two small harbors on the islands of Oahu and Maui. Data from bottom mounted pressure sensors at strategic locations inside and outside the harbors was analyzed and compared with the amplifications of the long-period waves computed from a mild-slope model. These types of measurements also allows for calibration of numerical and physical models.

Although numerical models are becoming well accepted in the planning of harbors, physical modeling cannot be ignored, particularly in complex situations where the validity of the mathematical approach may become questionable. Figure 1-2 shows the physical model for Barbers Point Harbor. Physical models, by nature, handle the refraction-diffraction and nonlinear interaction through scale modeling and generally represent the shorter-period waves more accurately than numerical models. Special care is required to properly generate long waves, because once generated, they tend to produce undesirable reflections from basin walls (Lillycrop et al., 1993 and Lee, 1985). Furthermore, the harbor and surrounding coastal areas are sculpted in cement in a three-dimensional model basin. Limitations to physical modeling include high cost, the lack of direct simulation of frictional dissipation, and the difficulties in working with long waves in an enclosed basin.

1.2.2 Numerical Models

Numerical models have been used to supplement and prepare for physical model tests. The results can be used to select wave gauge locations and identify promising alternatives for physical model tests. Although numerical models require some theoretical and computing skills from the operator, the implementation is far more convenient compared to their experimental counterparts. For instance, the harbor layout in a numerical model can be easily modified and tested compared to the time-consuming and costly re-construction of the physical model. Numerical models are also more efficient when unusually large areas or very long waves need to be simulated. In comparison to physical model tests, numerical models provide more accurate solutions for resonant modes with periods greater than 100 sec (Sand, 1982; and Lillycrop et al., 1993).

Various numerical models have been developed to study harbor resonance problems. The Helmholtz equation model was developed for harbor oscillations with constant depth, while Chen and Mei (1974), Berkhoff (1976), Houston (1981), and Xu and Panchang (1995) adopted the mild-slope models for wave agitation and harbor resonance in water of varying depth. Linear models, such as HARBD and the most recent CGWAVE (Demirbilek and Panchang, 1998), which use the elliptic mild-slope equations, remain the tool of choice by the Army Corps of Engineers. They are known as steady-state models that provide the solution in the frequency domain. These linear models are effective in providing harbor resonance frequencies and oscillation modes, but do not reproduce the actual generation mechanism associated with nonlinear wave-wave interactions.

Most harbors have dimensions much larger than the wavelength of the dominant wave frequency and the first few modes of oscillations are primarily excited by the subharmonics generated through nonlinear interactions. These subharmonics exist as forced waves, which are phase-locked to the primary waves, or free waves as the energy

of the primary waves dissipates through breaking or bottom friction. The primary waves in the harbor also interact with the oscillation through nonlinear energy transfer. Boussinesq models can provide a fairly comprehensive description of these nonlinear interactions (e.g., Chen and Liu, 1995; Nwogu and Demirbilek, 2001; and Lynett et al., 2002). These models provide solutions in the time domain and allow the user to capture the evolution of the waves over the entire time of simulation. In particular, Nwogu and Demirbilek applied an improved version of Nwogu (1996) to study the oscillation problems at Barbers Point Harbor.

1.3 Proposed Work

Barbers Point and Kahului are small harbors respectively on Oahu and Maui as shown in Figure 1-3 and have experienced occasional long-period oscillation problems. Over the last two decades, engineers and scientists from government agencies and academic institutions have conducted numerical and physical model studies of the oscillation in these two harbors (e.g., Palmer, 1970; Durham, 1978; Briggs et al., 1992; Okihiro et al., 1993; Lillycrop et al., 1993; and Nwogu and Demirbilek, 2001). All the numerical tests, with the exception of Nwogu and Demirbilek, were generated using linear mild-slope models, which do not account for the nonlinear wave-wave interaction. Nwogu and Demirbilek examined Barbers Point Harbor with the Boussinesq-based model BOUSS-2D and compared the identified natural periods with those obtained from the linear model CGWAVE. Yet, they did not systematically look into the structure of the oscillation patterns at resonance.

This study examine the resonance periods and the associated oscillation patterns at Barbers Point and Kahului using the model COULWAVE, based on the extended Boussinesq equation model (Lynett et al., 2002). The use of a nonlinear model allows the generation of the harbor oscillation from specified wind wave or swell spectra. The field

measurements and linear model results of Okihiro and Guza (1996) and Lillycrop et al. (1993) at Barbers Point and Thompson and Demirbilek (2002) at Kahului provide comparison with the nonlinear model results and validation of COULWAVE. Unlike Barbers Point, which is bounded by near vertical walls, 50% of the coastline inside Kahului Harbor consists of beaches where swashing of the waterline has to be properly modeled. The impact of a moving waterline on the oscillation patterns has never been examined before. The model of Lynett et al. has a provision for moving waterline and its application to Kahului Harbor provides new results in harbor oscillation studies.

2. BOUSSINESQ MODEL

2.1 Historical Development

Accurate prediction of nearshore wave conditions needs to incorporate both nonlinear and dispersive effects. Important wave processes need to be considered include diffraction, refraction, shoaling, and harmonic or wave-wave interaction. The Boussinesq equations were first developed to explain experimental observations of solitary waves, which could travel for relatively large distances without changes in their shape and speed. The classical form of the weakly nonlinear and weakly dispersive Boussinesq equations was derived by Peregrine (1967). Since both frequency dispersion and nonlinear effects are weak, the Boussinesq equations are not applicable to very shallow water, where the nonlinearity becomes more important than the frequency dispersion. Likewise, they are not applicable in deep water, where the frequency dispersion is of the first order. Finally, the equations could only resolve wave transformation for small amplitude waves, because of the weakly nonlinear term.

Madsen et al. (1991) modified the dispersive terms of the Boussinesq equations to extend the applications to shorter waves, or in deeper water. Nwogu (1993) extended the applicable range to deeper water by re-deriving the equations in terms of the velocity at an arbitrary vertical distance z_α from the still water level, instead of the depth-average velocity used by Peregrine (1967). The value of z_α becomes a free parameter, which is chosen to optimize the linear dispersion characteristics. Nwogu's alternative form of the Boussinesq equations significantly improved the linear dispersion properties of the original equations by making them applicable to a wider range of water depths. Despite the improvement in the frequency dispersion characteristics, the equations are based on the assumption that the wave heights are much smaller than the water depth, thus limits the ability of the equations to describe highly nonlinear waves in shallow water.

The modeling capability was greatly improved by the development of a fully nonlinear form of the Boussinesq equations by Liu (1994) and Wei et al. (1995). The new equations are particularly useful for simulating highly asymmetric waves in shallow water, wave-induced currents, wave setup close to the shoreline, and wave-current interaction. Furthermore, the extended Boussinesq equations can model the evolution of water waves from deep to shallow water. More recently, Lynett et al. (2002) extended the model of Wei et al. to include wave swashing. The model is known as Cornell University Long and Intermediate Wave model (COULWAVE) and has a robust treatment of the moving boundary and therefore is used in this study to model harbor oscillation.

2.2 COULWAVE

2.2.1 Governing Equations

A Boussinesq model provides a wave-by-wave simulation of the processes in the time domain, thereby providing an accurate description of the wave conditions in the surf and swash zone. The fully nonlinear and weakly dispersive model COULWAVE was developed at Cornell University. It is a Boussinesq-type equation model that allows for the evolution of fully nonlinear and weakly dispersive long and intermediate waves over variable bathymetry with a moving boundary for the changing waterline (Lynett et al., 2002).

The governing equations utilized by COULWAVE are derived by Wei et al. (1995) and are commonly referred to as the WKGS equations. The depth-integrated equations, in dimensionless form and Cartesian coordinates, are given as

$$\eta_t + \nabla\cdot\left[(h+\varepsilon\eta)\mathbf{u}_\alpha\right] - \mu^2\nabla\cdot\{(h+\varepsilon\eta)\left[\frac{1}{6}\left(\varepsilon^2\eta^2 - \varepsilon\eta h + h^2\right) - \frac{1}{2}z_\alpha^2\right]\nabla(\nabla\cdot\mathbf{u}_\alpha) + \left[\frac{1}{2}(\varepsilon\eta - h) - z_\alpha\right]\nabla[\nabla\cdot(h\mathbf{u}_\alpha)]\} = O(\mu^4) \tag{2.1}$$

$$
\begin{aligned}
&\mathbf{u}_{\alpha t} + \varepsilon \mathbf{u}_\alpha \cdot \nabla \mathbf{u}_\alpha + \nabla \eta + \mu^2 \left\{ \frac{1}{2} z_\alpha^2 \nabla (\nabla \cdot \mathbf{u}_{\alpha t}) + z_\alpha \nabla [\nabla \cdot (h \mathbf{u}_{\alpha t})] \right\} \\
&+ \varepsilon \mu^2 \{ [\nabla \cdot (h \mathbf{u}_\alpha)] \nabla [\nabla \cdot (h \mathbf{u}_\alpha)] - \nabla [\zeta (\nabla \cdot (h \mathbf{u}_{\alpha t}))] + (\mathbf{u}_\alpha \cdot \nabla z_\alpha) \nabla [\nabla \cdot (h \mathbf{u}_\alpha)] \} \\
&+ \varepsilon \mu^2 \left\{ z_\alpha \nabla [\mathbf{u}_\alpha \cdot \nabla (\nabla \cdot (h \mathbf{u}_\alpha))] + z_\alpha (\mathbf{u}_\alpha \cdot \nabla z_\alpha) \nabla (\nabla \cdot \mathbf{u}_\alpha) + \frac{z_\alpha^2}{2} \nabla [\mathbf{u}_{\alpha \cdot} \cdot \nabla (\nabla \cdot \mathbf{u}_\alpha)] \right\} \\
&+ \varepsilon^2 \mu^2 \nabla \left\{ -\frac{\eta^2}{2} \nabla \cdot \mathbf{u}_{\alpha t} - \eta \mathbf{u}_{\alpha \cdot} \cdot \nabla [\nabla \cdot (h \mathbf{u}_\alpha)] + \eta [\nabla \cdot (h \mathbf{u}_\alpha)] \nabla \cdot \mathbf{u}_\alpha \right\} \\
&+ \varepsilon^3 \mu^2 \nabla \left\{ \frac{\eta^2}{2} \left[(\nabla \cdot \mathbf{u}_\alpha)^2 - \mathbf{u}_\alpha \cdot \nabla (\nabla \cdot \mathbf{u}_\alpha) \right] \right\} + \mathbf{R}_f - \mathbf{R}_b = O(\mu^4)
\end{aligned}
\tag{2.2}
$$

where η denotes the free surface elevation and h the local water depth, and $\mathbf{u}_\alpha = (u_\alpha, \quad v_\alpha)$ is the reference velocity. The velocity is evaluated at the elevation $z_\alpha = -0.531h$, based on the optimum agreement of the governing equations with the linear dispersion relation as suggested by Nwogu (1993). The formulation is based on two dimensionless coefficients, $\varepsilon = a/h$ and $\mu = h/\lambda$, where a is the wave amplitude and λ is the wavelength. The coefficient ε is indicative of the importance of nonlinearity, while μ represents frequency dispersion and is a second order quantity. The parameterizations $\mathbf{R}_f$ and $\mathbf{R}_b$ account for the effects of bottom friction and wave breaking, respectively.

2.2.2 Wave Breaking and Bottom Friction

One of the most significant obstacles in developing a practical numerical model with depth-integrated equations is wave breaking. The Boussinesq equations do not have the necessary terms to account for wave breaking. Therefore, an eddy viscosity term $\mathbf{R}_b$ is added to the momentum equations to account for the energy dissipation due to wave breaking (e.g., Zelt, 1991; and Kennedy et al., 2000). This diffusive, second-order term is dependent on the wave slope. Since a depth-integrated model can only have a single surface elevation at a given horizontal coordinate, wave overturning cannot be simulated. The implementation of the eddy viscosity term is equivalent to treating all breaking waves as spilling breakers or bores.

Bottom friction is important in shallow water and is accounted for empirically through a friction coefficient f depending on the Reynolds number and seafloor condition. The bottom friction parameter is described in the quadratic form by

$$\mathbf{R}_f = \frac{f}{h+\eta} u_b |u_b| \tag{2.3}$$

where $(h + \eta)$ is the total water depth and u_b is the horizontal velocity at the seafloor. The above equation has been utilized in similar models (e.g., Chen et al., 2000). The bottom friction coefficient has a direct relation to the Chezy coefficient C as

$$f = \frac{g}{C^2} \tag{2.4}$$

where g is gravitational acceleration. The bottom friction coefficient typically is in the range of 10^{-3} to 10^{-2}.

2.2.3 Model Implementation

COULWAVE simulates wave propagation over a 2-D Cartesian grid with variable bathymetry. The numerical scheme utilizes a predictor-corrector time-stepping scheme, accurate to the fourth order (Δt^4) in term of the time step Δt. The finite difference scheme is accurate to the fourth order (Δx^4) in space, where Δx is the grid size, thereby minimizing numerical truncation errors in the spatial derivatives. The model simulates the moving boundaries in the swash zone using a numerical technique similar to that implemented by Kowalik and Bang (1987) for the nonlinear shallow-water equations. The moving waterline is modeled by extrapolating the solution from the wet region onto the beach. This linear extrapolation locates the position of the waterline between wet and dry nodes, thereby allowing the real boundary to exist in between grid points and improving the accuracy of the solution. The numerical results evaluated at the extrapolated waterline are used to update the solution for the next time step. This technique is numerically stable and does not require artificial dissipation.

The computational domain is analogous to a rectangular wave basin bounded by dissipative sponge layers placed along the walls. The sponge layer is modeled by dissipative terms in the governing equations that act to damp out the waves before they reach the boundary of the domain. Along a user-defined line within the computational domain, waves are generated using a source function approach. An algorithm converts the input wave spectrum into a time series of source functions that vary along the line to simulate the motion of a directional wavemaker. The free surface elevation along the line source is given by

$$\eta(x,y,t) = \sum_{i=1}^{M_\omega} \sum_{j=1}^{M_\theta} a_{ij} \sin[k_i(x\cos\theta_j + y\sin\theta_j) - \omega_i t + \phi_{ij}] \tag{2.5}$$

where a_{ij} is the discrete spectrum input, k_i is the wave number, ϕ_{ij} is a random phase shift, and M_ω and M_θ denote the number of frequency and direction bins respectively. Based on the approach of Wei et al. (1999), the internal source generates incident waves through addition and subtraction of mass along the line source. Individual mass fluxes for the components are computed at each time step and are summed accordingly to produce the prescribed surface elevation. Waves radiate out away from the line source in opposite directions. Those propagating toward the harbor are considered in the study; the sponge layers numerically absorb those propagating in the other direction.

2.3 Model Input

COULWAVE requires three input data sets. The first data set contains the bathymetry and topography of the area of interest. The second data set contains run-time and model parameters, which allow COULWAVE to generate the computational grid from the bathymetric and topographic input. The third data set contains the incident wave information. The input data sets and the generation of the computational grid are described in more detail in the following sections.

2.3.1 Bathymetry and Topography

The bathymetric and topographic data of the studied area must be organized in a rectangular grid with a user-defined origin. The data is contained in 4 files:

- x_topo.dat contains the locations of the grid points in meters along the x-coordinate from the point of origin to x_{max}. The increment between adjacent grid points should be kept constant.
- y_topo.dat contains the locations of the grid points in meters in the y-coordinate from the point of origin to y_{max}. The grid resolution should be the same as in x_topo.dat.
- size_topo.dat contains the number of points in x_topo.dat and y_topo.dat.
- f_topo.dat contains the water surface and land elevations in meters at the grid points. Negative values represent water depth. The data is arranged by row in the x direction starting at the origin.

The total number of grid points is equal to the product of the numbers of grid points in the x and y directions.

Some factors need to be considered in the selection of the grid boundaries and resolution. The size of the domain is selected so that the distance from the coastline to the offshore boundary is on the order of a few kilometers to provide sufficient time and distance for the waves to interact with each other. Additionally, the distance between the lateral boundaries should not be restricted to the width of the harbor; it is common practice to add a few hundred meters of additional bathymetry at each side of the harbor. The location of the offshore boundary is determined such that the maximum water depth is less than half the shortest wavelength of interest. In addition, the water depth must be kept uniform along the wave generation boundary. For very detailed and intricate bathymetric data containing numerous dips and rises, the resolution between the grid points should be kept at about 8 to10 m. This is due to the depth-averaged nature of the Boussinesq equations that gets less stable for complicated underwater relief.

2.3.2 *Simulation Parameters*

The model-setup and runup-time parameters for COULWAVE are stored in the ASCII text file sim_set.dat. The parameters in the file define the computational grid and simulation conditions. The key parameters include grid resolution, time step size, number of iterations per time step, type of governing equations, sponge-layer arrangement, wavemaker location, simulation time, and output interval as listed in Table 2-1.

The grid resolution is defined by the number of grid points per wavelength at the wavemaker location based on the peak period of the incident wave spectrum. The value should be in the range of 30 to 50 grid points per wavelength. The grid spacing should be chosen to resolve the shortest wave period in the shallowest part of the domain. Once the grid resolution is defined, the time-step size Δt is selected using the Courant number, which is defined as:

$$Cr = \sqrt{\left[C^2 \Delta t^2 \left(\frac{1}{\Delta x^2} + \frac{1}{\Delta y^2} \right) \right]} \tag{2.6}$$

where C is the phase speed calculated using the maximum water depth (h_{max}) and the peak period of the incident waves. For stability, the Courant number must be less than 1 with a typical value of between 0.4 and 0.7. In addition, the user needs to specify the maximum number of iterations per time step in the corrector loop.

The model can use the linear or nonlinear equations in the simulation. For the nonlinear case, the user can either choose the weakly or fully nonlinear equations. The weakly nonlinear equations of Nwogu (1993) are restricted for small amplitude waves, with the amplitude to depth ratio of the order O(0.1). The fully nonlinear model of Wei et al. (1995) allows for the simulation of waves with larger amplitudes at the expense of increasing CPU time due to the high-order terms in the governing equations. The weakly nonlinear equations, however, produce more stable computations.

The model automatically assigns a sponge layer along the boundary of the rectangular domain. The width of the sponge layer is specified by the user and is selected to dissipate the wave energy approaching the boundary and reduce reflection. Typical widths can be anywhere between $3/4L_{max}$ to $1¼L_{max}$, where L_{max} is the length of the longest waves generated by the wavemaker. Large values of L_{max} would reduce reflection, but at the expense of increasing CPU time. The wavemaker location is measured as distance from the offshore boundary. In addition, the user needs to specify the simulation time and output interval in second.

2.3.3 Wave spectrum data

The program can generate regular or bichromatic incident waves. For irregular waves, the user needs to supply a directional spectrum as part of the input. Measured spectral wave data can be obtained on-line from the National Ocean Administration Agency (NOAA) National Data Buoy Center (NDBC). Since the number of offshore buoys is limited due to their high cost of operation, measured data is usually unavailable at the location of interest.

Most practical applications use numerically generated spectral data or a parametric spectrum based on given significant wave height and peak period. There are a number of global and regional wave models in operation. These operational models are mostly based on WAM (WAMDI, 1988) or WAVEWATCH (Tolman, 1989), which provide directional wave spectra in deep water. The deep-water data can in turn be used as input for a near-shore wave model such as SWAN (Booij et al., 1996). If site-specific wave conditions such as the significant wave height and peak period are known, it is possible to generate the incident wave conditions for the model using parametric spectra (e.g., Bretschneider, 1959; Hasselmann et al., 1973).

The Bretschneider spectrum is one of the most commonly used in engineering applications. It has the same shape as the Pierson-Moskowitz spectrum (Pierson and

Moskowitz, 1964), but is more conveniently defined in terms of the significant wave height, H_s, and peak frequency, f_p, as

$$S(f) = \frac{5H_s^2}{16} \frac{1}{(f/f_p)^5} \exp\left[-\frac{5}{4} \left(\frac{f}{f_p} \right)^{-4} \right] \tag{2.7}$$

Figure 2-1 shows an example of the Bretschneider wave spectrum with H_s = 0.5m and T_p = 15 sec. Most parametric wave spectra do not contain information on direction spreading, which can be accounted for by a directional spreading function (e.g., St. Denis and Pierson, 1953). In the numerical simulation, the input wave spectrum is truncated at 5% of the peak energy.

2.3.4 Computational Considerations

Once the program starts, it interpolates the bathymetric and topographic grid to generate a computational grid based on the user-specified number of grid points per wavelength. As mentioned in the previous section, the grid resolution gets finer as the number of grid points per wavelength increases. The coverage of the computational domain is slightly larger than that of the bathymetric and topographic grid, because of additional damping regions along the sides. The computational grid still follows the x-y coordinate system of the bathymetric grid, but with a shifted origin and has uniform grid spacing Δx and Δy.

The maximum size and resolution of the computational domain should be based on the available computational resources. For a Pentium 4 PC with a 3.06-GHz processor and a 1-GB physical memory, the grid size should not exceed 1000×1000. With the Intel FORTRAN Compiler, the computational speed is about 0.1 minute per time step using the fully nonlinear set of equations. A typical 30-minute simulation requires 10,000 time steps and generates approximately 4 GB of data. Smaller grids can be used and results in much less CPU time and storage requirements.

2.4 Data Output and Analysis

2.4.1 Data Files

COULWAVE calculates the time-dependent evolution of the water-surface elevation and horizontal velocity over the domain and outputs the results over the computational grid. The output data is written in ASCII text files, which are described as follow:

- x1.dat contains the x computational grid locations.
- y1.dat contains the y computational grid locations.
- time.dat contains the times when the output is written to the file.
- depth1.dat contains the computational grid including the sponge-layer regions. The water depth or land elevation over the entire grid is written in one column. The data is arranged by row in the x direction (alongshore) starting at the origin.
- zeta1.dat contains the time-history of the free surface elevation over the domain at the requested output interval. The format is the same as depth1.dat.
- bl_visc1.dat contains time histories of the grid status (wet/dry) as well as the dissipation by wave breaking at the output interval.
- uv1.dat contains the time history of the flow velocity vector (u,v) at the output time interval. The first and second columns contain respectively the u and v vector fields.

2.4.2 Data Analysis

COULWAVE outputs a large volume of data that must be processed to extract the relevant information. Following the model simulation, a few additional steps are necessary to generate the harbor response spectrum and to identify the natural oscillation modes. Figure 2-2 illustrates the steps involved in the data analysis. The five output data files (bl_visc1.dat, depth1.dat, x1.dat y1.dat, and zeta1.dat) are post-processed with Matlab to extract the frequency spectrum in the harbors and to re-format the data for the visualization software Tecplot.

At the end of the simulation, the time history of the water surface elevation over the entire simulation is available. The discrete Fast Fourier Transform (FFT) generates the frequency spectra for all selected grid points. The space-averaged response spectrum of the harbor is given by

$$S(f) = \frac{1}{N}\sum_{i=1}^{N} S_i(f) \tag{2.8}$$

where f is frequency, N is the number of grid points inside the harbor, and $S_i(f)$ is the discrete spectrum at grid point i. As compared to previous studies, which examine the response at discrete locations, this space-averaged spectrum provides a more complete description of the harbor oscillation characteristics. The harbor natural periods, in principle, can be identified from the peaks of the normalized spectrum. The contour plot of the oscillation amplitude at a specific period can be obtained from the discrete spectra at the grid points.

The resolution of a spectrum is determined by a number of factors. Numerically, the length of the time series controls the resolution of the spectrum generated from the Fast Fourier Transform. Due to the relatively short simulation time, the FFT algorithm automatically zero-pads the input time series to increase the resolution of the output spectrum. This allows the user to determine more precisely the frequencies at which the major peaks of energy appear.

3. RESULTS AND DISCUSSION

3.1 Harbor Descriptions

3.1.1 Barbers Point Harbor

Located between 19° and 22° North latitude, Hawai'i is the southernmost state in the United States. Figure 3-1 illustrates the wave climate of Hawaii. Waves from the northeast are generated by the trade winds. During the summer months, waves originating from the Southern Hemisphere approach Hawaii from the southwest. The largest waves occur during the winter and are caused by storms in the Northwest Pacific Ocean. Barbers Point is located on the southwest side of the island of Oahu approximately 24 km west of Honolulu Harbor. It is the newest of nine commercial cargo-handling facilities in the Statewide Commercial Harbor System. The aerial picture in Figure 3-2 shows that the harbor is artificial and can be classified as the "Inland Basin" type. Except for the entrance channel, the harbor complex is situated completely inland from the shoreline. This minimizes the impact on coastal resources and eliminates the need for protective structures.

The planning of the harbor started in 1958 when Congress ordered a study to determine the feasibility of a second harbor on the island of Oahu. In 1961, developers of the adjacent industrial park constructed a small L-shaped barge harbor to enable transport of products directly to other islands. Because of its limited size and seiche problems, the harbor had limited commercial use and was more popular for recreational fishing. Congress authorized the construction of Barbers Point Harbor under the River and Harbor Act in 1965 and appropriated construction funds in 1979. The University of Hawaii, under a contract from the USACE Pacific Ocean Division (POD), conducted a hydraulic model study (Lee, 1985). All design plans incorporated a small boat harbor extending off the deep-draft harbor basin. The U.S. Army Engineer Waterways Experiment Station

(WES) evaluated the effects of the small boat harbor and examined the proposed deep-draft harbor.

The construction of the deep draft harbor was finally completed in 1985 and the small boat harbor in 1989. Figure 3-3 shows the layout of the complex, which consists of an entrance channel, a barge basin, a deep-draft harbor, and a small boat harbor. To reduce the wave energy entering and becoming trapped in the harbor, 1400 km of rubble-mound wave absorbers were placed on either side of the entrance channel and along the divider between the deep-basin and the small boat harbor. The rock size varies from 0.5 ton to 1 ton at the innermost section of the harbor basin and increases to 2 ton to 4 ton towards the seaward sector of the harbor. The deep-harbor accommodates containerships, tankers, bulk carriers, and barges. The small boat harbor is located northwest of the deep-draft basin and was designed to accommodate 350 to 500 small crafts.

Figure 3-4 shows the input bathymetric and topographic grid for Barbers Point. The land topography is not shown in the figure so that the coastline and bathymetry can be clearly seen. The entrance channel is 1300 m long, 140 m wide, and 12.8 m deep and the alignment is approximately 74° from the shoreline. The bottom contours outside the harbor are relatively parallel. The channel was excavated from the bedrock with a 1:1 side slope from the seaward end to the shoreline and with a 1:1.5 slope from the shoreline to the basin. The water depth offshore of the 25-m contour is treated as uniform for the operation of the wavemaker. Figure 3-5 provides a close-up view inside the harbors. The deep-draft basin is approximately 700 m by 640 m and 12.8 m deep. A shallow, small boat marina 4 to 5 m deep connects to the deep-draft harbor through a channel near the main harbor entrance. Water surface measurements at the locations indicated in the figure are available for extended periods. Although the deep-draft basin was recently extended, this case study uses the 1989 configuration of the harbor so that comparison can be made with previous field measurements and numerical results.

3.1.2 Kahului Harbor

Kahului Harbor is situated on the north shore of Maui at the apex of a large V-shaped bay, two miles from Wailuku, Maui's largest town and the county seat. It is the busiest Neighbor Island port in the State and is the only commercial port that serves ocean cargo vessels for the Island of Maui. The Kahului Railroad Company began construction of a protective breakwater in an exposed inlet at Kahului in the early 1900's. In 1910, the Corps of Engineers received authorization to improve the breakwater and dredge the harbor. Additional improvements and modifications were made over the years, with the completion of the deep-draft harbor in December 1931.

Figure 3-6 shows an aerial picture of Kahului Harbor, which is separated from the open ocean by two breakwaters and belongs to the classification of "Protected harbors". The breakwaters are armored with concrete units of up to 35 tons on the trunk and 50 tons on the head for protection against severe winter swells. A total of 920 m of commercial piers is located in the eastern part of the harbor as shown in Figure 3-7. The Piers are used by a variety of vessels including barges, container ships, passenger cruise ships, and tugboats. The 405-m long Pier 1 accommodates up two ocean-going vessels. Piers 2 and 3 accommodate barge activities. Two canoe clubs are located along the shore immediately southwest of Pier 2. The southern shore of the harbor, between the boat ramp and canoe clubs, includes a revetment along Kahului Beach Road and several rock groins further East. A large coral stockpile has been placed inside the harbor, adjacent to the West breakwater. This area, under the jurisdiction of the County of Maui, is being considered for park development.

Figure 3-8 shows the bathymetric and topographic grid. The ship basin, which is defined by the 11-m contour, is approximately 730 m long and 600 m wide alongside Pier 1 on the east side of the harbor. Okihiro et al. (1993) deployed a pressure sensor near Pier 1 and another one off the east breakwater, as indicated in the figure, to investigate harbor

oscillation. The southwest part of the harbor is shallow with beaches lined along the coastline. The 200 m wide entrance faces northward and is bounded by the two breakwaters. Directly offshore of the harbor entrance the depth is 10 to 12 m. The offshore bathymetry is complicated; east of the harbor entrance, shallow areas of less than 3 m deep extend 1 to 2 km offshore, whereas to the west the bottom slope is steeper and relatively constant. The water depth offshore of the 25-m contour is treated as uniform for the operation of the wavemaker.

Zeki Demirbilek from the U.S. Army, Engineer Research and Development Center, Coastal and Hydraulics Laboratory (ERDC-CHL) provided the bathymetric data for Barbers Point and Kahului harbors and their surroundings. The data was initially obtained from the Scanning Hydrographic Operational Airborne Lidar Survey (SHOALS) surveying system, which was carried out as part of a joint study by the U.S. Army Corps of Engineers and the Scripps Institution of Oceanography, University of California, San Diego. The SHOALS data appears to give accurate and detailed coverage inside and outside the harbor, when compared with the hydrographic charts of the National Oceanic and Atmospheric (NOAA) and the National Ocean Service (NOS) hydrographic charts. The data from ERDC-CHL contains the measurements of the water depth inside and outside the harbors. Since COULWAVE can model wave swash and requires the topography as well, land elevations adjacent to the harbor are obtained from topographic maps.

3.2 Sensitivity Tests

The computed results depend on a number of assumptions and parameters, which need to be examined to assure the quality of the results. These include the use of a parametric wave spectrum, the resolution of the wave spectrum, and the duration of

simulation. These are examined in the following sections using Barbers Point Harbor as an example.

3.2.1 Bichromatic Wave Input

This sensitivity test examines the model's ability to generate subharmonic and superharmonic waves due to nonlinear wave-wave interaction. The wavemaker is programmed to generate a bichromatic wave train with periods of 14 and 14.9 sec. Figure 3-10 shows the time series of the surface elevation at a node near the wavemaker. The time series shows significant modulation of the wave amplitude with a period of about 210 sec. This is due to the constructive and destructive interference between the two wave components. The spectrum of the time series clearly shows the high energy at these two frequency components.

Figure 3-11 illustrates the time series of the water elevation and the frequency spectrum at a selected point on the east side of Barbers Point Harbor. This time series does not appear to be as structured as the time series near the wave maker. Furthermore, the water surface elevation is lower inside the harbor because only a portion of the incident wave energy gets into the harbor. The computed spectrum clearly shows additional frequency peaks on the lower and higher ends of the spectrum with even more energy than the primary waves at 14 and 14.9 sec. These waves correspond to the subharmonics and superharmonics generated from the primary input waves. This shows the model capability of generating the higher and lower harmonic waves from nonlinear wave-wave interaction.

3.2.2 Simulation Time

In principle, the longer the simulation time, the better the resulting spectrum is to capture the long-period oscillations. A test was performed to determine the minimum simulation time to capture the natural modes inside Barbers Point Harbor. A wave train

with a significant wave height of 0.5 m and a peak period of 16 sec is simulated for 15, 30, and 45 min and the respective wave spectra are compared.

Figures 3-12a to 3-12c show the space-averaged spectra inside the harbor for the 15-min, 30-min, and 45-min runs. The results are computed using a resolution of 0.0005 Hz in the input wave spectrum. The most energetic peak for the 15-min run appears at 540 sec, while the peaks for the 30-min and 45-min runs appear at 990 and 1010 respectively. The difference between the 15-min and other runs is attributed to the short simulation time, which is barely sufficient to capture one cycle of the oscillation. In addition, it takes a few minutes for the basin to reach steady-state oscillation from the start of the simulation. As the simulation time increases, the individual peaks appear to be narrower and more resolved due to a reduction of noise. The lowest mode of oscillation for the 30 and 45 min simulations appears at a period of about 1000 sec. It is therefore unnecessary to run the model for a simulation time longer than 30 min.

3.2.3 Wave Spectrum Resolution

Harbor oscillation is excited by long-period waves generated by nonlinear interaction among wave frequency components. The incident wave spectrum is discretized into a finite number of frequency components before being input to the wavemaker. The resolution of the input spectrum affects the generation of nonlinear long waves and the resulting oscillation in the harbor, and needs to be investigated before the model is applied more generally to determine the natural modes. Figures 3-13a to 3-13c show the space-averaged spectra obtained from an incident wave spectrum with 0.005, 0.001, and 0.0005 Hz resolutions. The results are computed for a 30-min simulation with an incident wave spectrum for $H_s = 0.5$m and $T_p = 18$sec.

Figure 3-13a shows an interesting pattern with the high-energy peaks at constant intervals corresponding to the input spectrum resolution of 0.005 Hz. The long waves or subharmonics are primarily generated through second-order interactions between the

frequency components in the input wave spectrum. These long-wave components have frequencies equal to the frequency differences of the components or literally at multiples of the input spectrum resolution. These dominant peaks, therefore, may not represent natural oscillations. The smaller peaks surrounding the dominant peaks likely represent true natural oscillations, which are excited by the weaker, higher-order components. Despite the coarse resolution of the input spectrum, the model is capable of identifying resonance at a higher resolution.

The oscillation spectrum in Figure 3-13b is based on a finer resolution of $\Delta f = 0.001$ Hz in the input wave spectrum. The dominant peaks increase in number, but are still evenly distributed following approximately the input resolution. However, most of the peaks are shifted slightly from the frequencies of the incident long-wave components and some of the high-energy peaks in Figure 3-13a become almost non-existent at this resolution. At an even finer resolution of $\Delta f = 0.0005$Hz, the results are greatly improved as shown in Figure 3-13c. The peaks no longer evenly distributed following the input resolution and more likely to represent natural oscillations of the harbor. However, the true resonance still needs to be confirmed by an evaluation of the oscillation pattern. The spectral resolution can, in theory, be further refined infinitesimally, but this leads to instability of the Boussinesq model. Therefore, the resolution of 0.0005 Hz is used to model the incident wave spectrum.

3.3 Oscillation and Resonance

3.3.1 Incident Wave Conditions

The natural frequencies and the respective oscillation patterns at Barbers Point Harbor are examined for two sets of incident wave conditions corresponding to

- $H_s = 0.5$ m, $T_p = 16$ sec
- $H_s = 0.5$ m, $T_p = 18$ sec

The response of the harbor is simulated for 30 min with unidirectional incident waves. Thompson and Demirbilek (2002) studied Barbers Point and Kahului harbors with the steady-state linear model CGWAVE (Demirbilek and Panchang, 1998) and concluded that the long-period oscillation in the harbors is independent of the direction of the approaching waves. Therefore, the simulation for the harbor was conducted with an incident wave angle of 90 degrees with respect to the shoreline.

The sensitivity tests have shown that the propagation of the incident waves toward the shore results in the generation of a set of sub-harmonic waves through nonlinear wave-wave interaction. These second-order components have frequencies equal to the sum and difference between the input wave frequencies. Higher-order terms are also generated, but with smaller amplitudes. Therefore, the primary input wave characteristics play a significant role in the generation of the sub-harmonics, which in turn affect the response of the harbor analogous to a damped oscillator. In addition, the primary waves might interact with the harbor oscillation, modifying its response characteristics. Two input wave spectra with different peak periods are therefore used in the simulation to determine the effects of the primary waves on the long-period oscillation characteristics.

3.3.2 Barbers Point Harbor

Okihiro et al. (1993) deployed four near-bottom pressure sensors inside the harbor and one outside the harbor as indicated in Figures 3-4 and 3-5. The sensors are indicated with a letter that corresponds to their geographical location in the harbor (i.e. E for East). The instruments recorded the water elevation 4 times per day for about 4 hours at a 0.5 Hz sampling rate. They gathered 5 months of data and presented the time-average power spectra of water elevation inside the harbor with a frequency resolution of 2.4×10^{-4} Hz. The presented spectra are normalized with the wave spectrum outside the harbor and correspond to the transfer functions of the long-period wave components. The measured data was compared with linear model results generated with a fine resolution of 3.8×10^{-6}

Hz and averaged over possible incident wave directions and over frequency to match the frequency resolution of the field data.

Figures 3-14a to 3-14d compare the normalized wave spectra obtained from COULWAVE at the four locations with the results presented by Okihiro et al. (1993). Both the normalized spectra from COULWAVE and the field data produce the highest peak around 1000 sec, which represents the lowest mode of oscillation known as the grave or pumping mode. The computed spectra at the 16 and 18-sec excitation periods follow the general trends with some shift in the response frequency and amplitude. The spectral peak period affects the energy of the sub-harmonics, giving rise to different response amplitudes. The frequency shift indicates the effects of the excitation period on the long-period oscillation modes. The frequencies of the dominant peaks, except for the grave mode, vary with locations in the harbor and are associated with the pattern of nodes and antinodes. The comparison between the computed and measured spectra is reasonable with corresponding dominant peaks and troughs. The discrepancies are expected because the measured spectra correspond to seasonal averages and are normalized with the subharmonics outside the harbor that are generated naturally and might have different characteristics as those generated numerically in a confined domain. Similar shifting between the measured and linear model results is also observed and was believed to be the result of bathymetry change due to the accretion of sediments (Okihiro et al., 1993).

Figure 3-15 compares the space-averaged spectra inside the harbor with the spectra at the outside gauge location for the 16 and 18-sec wave excitations. The results are presented for the frequency range from 0.0008 to 0.025 Hz, which covers all possible periods of oscillation from 40 to 1200 sec including the grave mode. The harbor response spectra for the 16 and 18-sec peak period are quite similar in shape and exhibit similar periods of the natural modes. Both show the grave mode at around 0.001 Hz (1000 sec)

and dominant peaks at about the same frequencies. The long-period oscillation inside the harbor seems to be correlated to the subharmonics outside the harbor. The difference of energy levels inside and outside the harbor is greater at low frequencies, because of the natural oscillations that amplify the low-frequency energy level inside the harbor. The energy-level difference diminishes with increasing frequency and the two curves are expected to cross at higher frequencies, where the harbor is designed to reduce the energy of the primary waves.

The natural modes are defined by the location and the number of nodes and antinodes in the harbor. They are selected based on the sharpness and extent of the nodes and antinodes as well as the peaks in the space-averaged spectra. Some of the modes exhibit several variances of oscillation patterns that belong to the same general category. Since the spectral resolution is defined by frequency, the resolution in terms of oscillation period is distorted in favor of shorter periods. The results for periods longer than 300 sec might not precisely capture the natural oscillation modes. This, however, is not a major limitation of the analysis, since most of the oscillation periods are shorter than 200 sec. About 150 amplitude plots were generated from over the frequency range. About 10 natural oscillation modes were identified based on their distinct patterns and locations of nodes and antinodes. The results are shown in Figures 3-16 through 3-27 with decreasing resonance periods.

Figure 3-16 shows the grave mode, which is characterized by an almost uniform rise and fall of the water elevation in the harbor. The fundamental or first mode of oscillation, as shown in Figure 3-17, has a node at the entrance and an antinode at the east corner of the harbor. As the oscillation period decreases, the node migrates inward and a new antinode develops at the entrance forming the 2nd mode of oscillation as shown in Figure 3-18. This oscillation mode transforms into a new pattern as shown in Figure 3-19 with antinodes at the two sides of the entrance. Figures 3-18 and 3-19 show an interesting

coupling pattern, in which the nodes extend from the deep draft basin to the West Beach Marina despite the presence of the solid barrier. The higher oscillation modes are characterized by increasing number of nodes and antinodes. Most of the oscillation modes generated by the two wave spectra follow the same pattern and occur at similar periods. The difference between the two sets of results increases with decreasing oscillation period and may be attributed to the nonlinear interaction with the primary wave energy.

Lillycrop et al. (1993) analyzed the linear results obtained from an elliptic mild-slope model and identified seven oscillation modes. Their results are presented in Figure 3-28. Color patterns are added to the original plots in which the nodes and antinodes are shown in blue and red respectively. Both the linear and nonlinear models give the period of the grave mode around 1000 sec. The linear model predicts the fundamental mode at 585.1 sec, while the nonlinear model predicts the period at best around 480 sec. The next mode at 205 sec computed by the linear model has a node across the deep draft basin and the marina and two antinodes across the entrance to the harbor. The nonlinear model gives a similar pattern of oscillation at about 170 sec. This oscillation at 132 sec is often referred as the rocking mode, where the node extends from the east end of the harbor to the west and the antinodes fluctuate up and down on the north and south corners of the harbor. The nonlinear model captures a similar pattern at 129 sec. The next two modes at 107.8 sec and 85.3 sec were accurately reproduced by the nonlinear model at around the same period, but not the mode at 57.3 sec, where the nonlinear model does not produce the same results for the two incident wave spectra.

3.3.2 Kahului Harbor

Kahului Harbor has a different geometry compared to Barbers Point and offers a different perspective of the harbor oscillation problem. Okihiro and Guza (1996) conducted a field study to obtain the surface elevation spectra at the location of Pier 3 (●)

and outside the harbor (■) as indicated in Figure 3-8 and Figure 3-9. Figure 3-29 compares the computed spectra and the measurement, which have been normalized by the spectrum recorded outside the harbor. COULWAVE produces similar response spectra for the 16 and 18-sec excitations. The computed spectra also show similar general behavior as the measured data, which was averaged over a period of five months. Figure 3-30 compares the space-averaged spectra inside the harbor with the spectra at the outside gauge location for the 16 and 18-sec wave excitations. The grave mode occurs at about 900 and 1000 sec and has the highest amount of energy. The long-period oscillation inside the harbor seems to be correlated to the subharmonics outside the harbor.

Eight oscillation modes are identified from 140 response amplitude plots from 40 sec to 1200-sec periods. Figures 3-31 to 3-40 show the oscillation patterns arranged in decreasing resonance period. Since the South shore of the harbor consists of natural beaches where wave swashing may occur, the still water line provides a convenient definition of harbor boundary there. Similar to Barbers Point, the grave mode of Kahului as shown in Figure 3-31 corresponds to a near-uniform rise and fall of the water level. The fundamental or first mode in Figure 3-32 has a node at the entrance and increasing amplitude toward the south shore of the harbor. The high amplitude region near the south shore does not correspond to an antinode, because the water can move freely across the boundary. The rocking mode occurs around 160 sec and is characterized by a node arching from the east and west breakwaters. A second rocking mode occurs around 145 sec with the node perpendicular to the east breakwater. These two modes may significantly affect the operation at Pier 1, which is located along the east breakwater. A third rocking mode is observed around 115 sec with the node perpendicular to the west breakwater. The oscillation pattern becomes more complicated with additional nodes and anti-nodes.

Thompson and Demirbilek (2002) analyzed Kahului Harbor and identified 3 natural modes that have the most impact on harbor activities at the piers. Their results are presented in Figure 3-41. The oscillation modes simulated with the linear model at 181.8 sec and 58.5 sec do not have comparable matches with the COULWAVE results. The 121.1 sec mode has a node that extends from the east to the west breakwaters while crossing through Pier 2. An additional node is located close to the tip of the west breakwater. The nonlinear model was able to simulate a similar pattern of oscillation at 91 sec. The disagreement regarding the patterns of oscillation and their respective period between the two models is certainly attributed to the presence of the natural shoreline on the south shore of the harbor. As mentioned earlier, the nonlinear model is able to simulate the waves in the swashing zone, whereas CGWAVE considers the boundary as a impermeable vertical wall. The treatment of the boundary affects the overall flow pattern leading to different oscillation modes. The increasing importance of the nonlinear effects near the natural coastline further modifies the results in comparison to the linear model.

4. CONCLUSIONS

The present study applies a recently developed Boussinesq model to analyze the long-period oscillation of Barbers Point and Kahului Harbors. Two Bretschneider spectra with different peak periods provide the incident wave conditions. The long-period waves, which are generated through nonlinear wave-wave interaction, provide excitation to the harbor. Using the Fast Fourier Transform, the response spectra are computed from the surface elevation time series and averaged over the harbor to provide a general indication of the response.

A sensitivity analysis shows that a simulation time of 30 min is sufficient to capture all the oscillation modes, including the grave mode or the lowest mode of oscillation. A frequency resolution of 0.0005 Hz or less in the incident wave spectrum is necessary to produce better resolution of the response spectral peaks. The comparisons of the response spectra inside Barbers Point Harbor and Kahului Harbor with field measurements and linear model results indicate reasonable agreement. Furthermore, the energy at resonance inside the harbor shows good correlation with that of the offshore long waves. The data indicates that the spectral peaks might not exactly correspond to the natural oscillation modes with well-defined nodes and antinodes. Aided by the space-averaged response spectrum, the oscillation modes are identified from the response amplitude plots.

The data produces 12 and 10 natural oscillation modes respectively for Barbers point and Kahului harbors over the frequency range of 40 to 1200 sec. The longer period oscillation modes at Barbers Point show very good agreement with published linear model results, except for the rocking mode around 132 sec. The present study also identifies additional modes that were not identified in previous studies. The computed oscillation modes at Kahului, however, do not agree with published linear model results. This could be due to the swashing mechanism in COULWAVE that allows water to move

freely onto dry land, providing an accurate description of the boundary condition. Linear models, on the other hand, treat the boundary surrounding the harbor as a vertical wall. In addition, the diminishing water depth toward the shoreline gives rise to important nonlinear effects, which cannot be accounted for with the linear model.

This study shows that the fully nonlinear and weakly dispersive Boussinesq model can accurately and efficiently generate the natural oscillation modes of harbors. The model can be used in conjunction with physical model tests to provide a complete and realistic description of harbor oscillation problems.

Table 2-1: Barbers Point and Kahului Harbors Simulation Parameters.

Parameter	Value
Number of grid points per wavelength	40
Time Step Size (sec)	3
Simulation Time (sec)	1800
Fully Nonlinear Simulation	on
Wave breaking model	on
Width of Sponge Layer in Wavelength	1
Maximum iterations	200
Minimum iteration(s)	1
Corrector stage convergence error	5.00000024E-04
Bottom friction coefficient	0.03

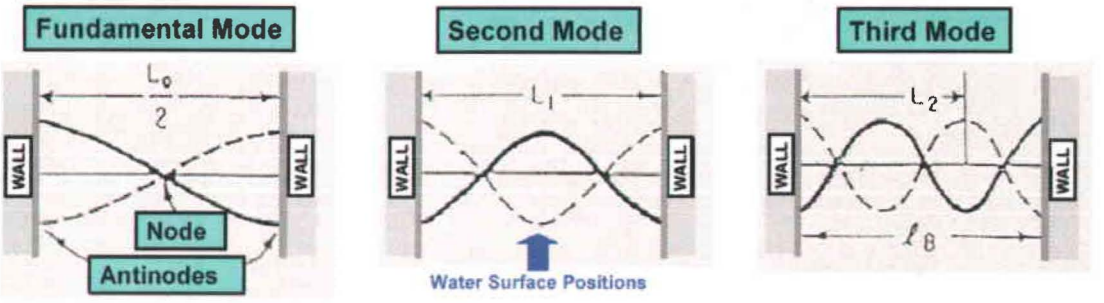

Fig. 1-1: Basin Oscillation Definition.

Fig. 1-2: Barbers Point Physical Model (http://chl.wes.army.mil).

Fig. 1-3: Hawaiian Islands Map.

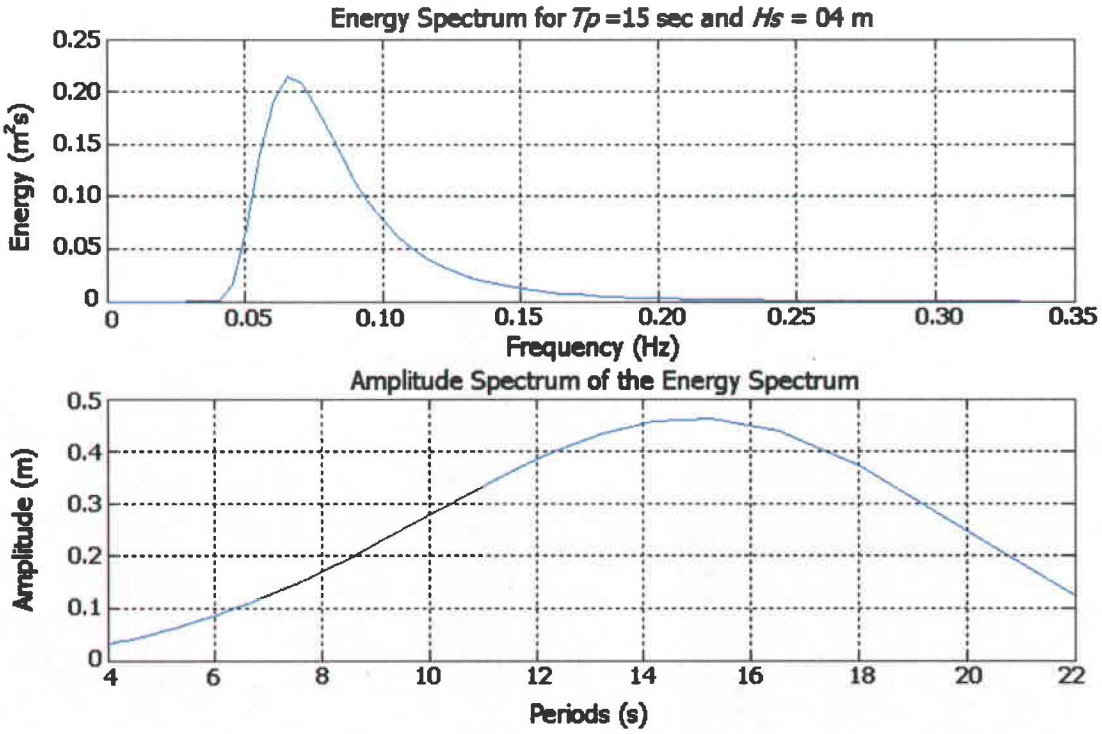

Fig. 2-1: Energy and Amplitude Spectrum from Bretschneider Wave Spectrum with $H_s = 0.4$ m and $T_p = 15$ sec.

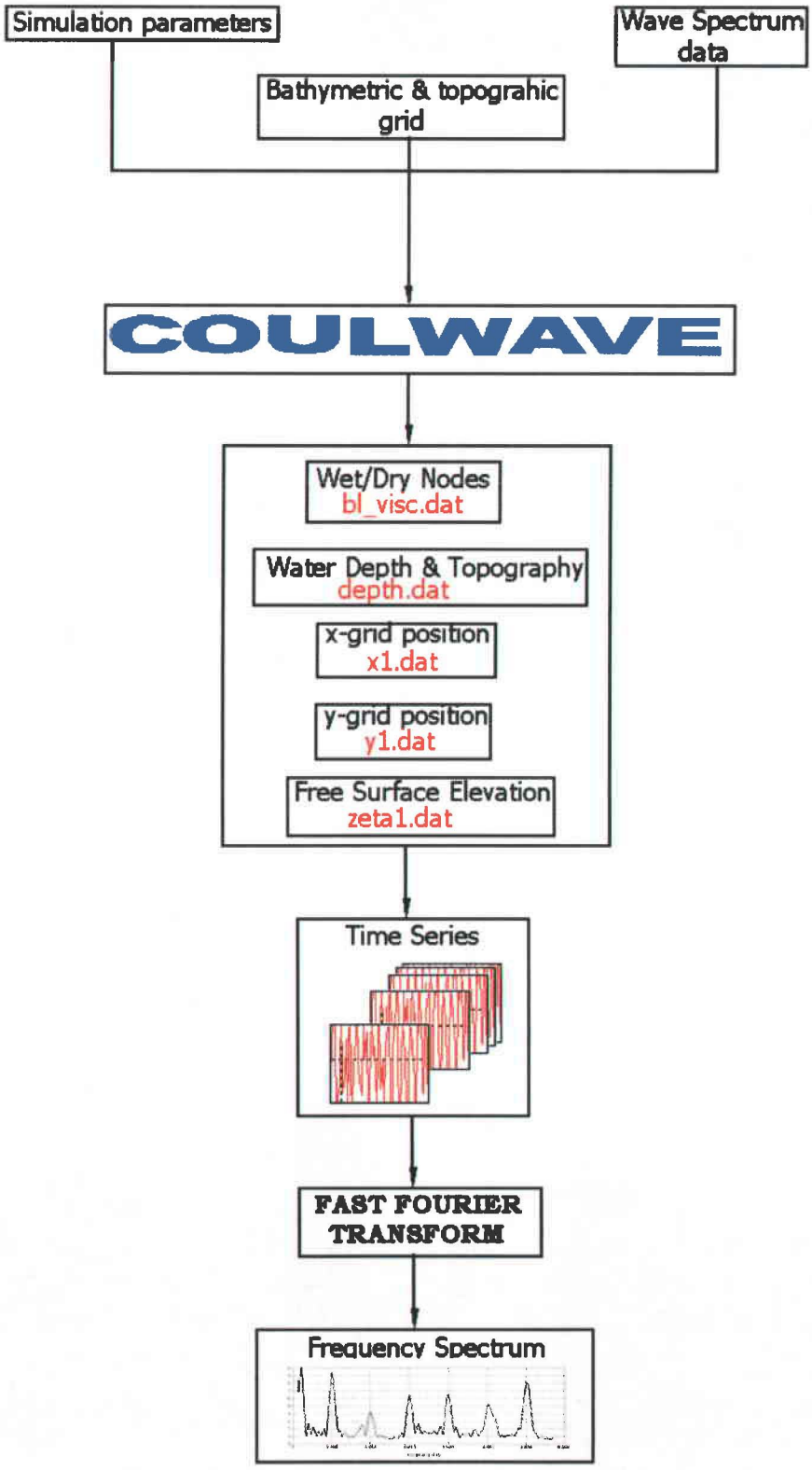

Fig. 2-2: COULWAVE Data Framework.

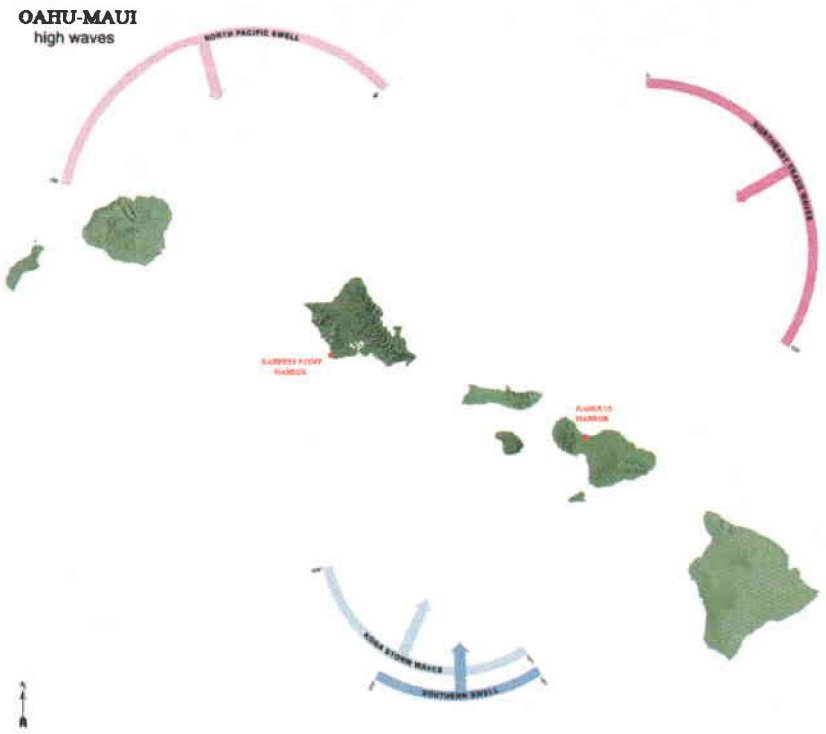

Fig. 3-1: Oahu and Maui Wave Climate.

Fig. 3-2: Barbers Point Harbor Aerial View (http://www.state.hi.us).

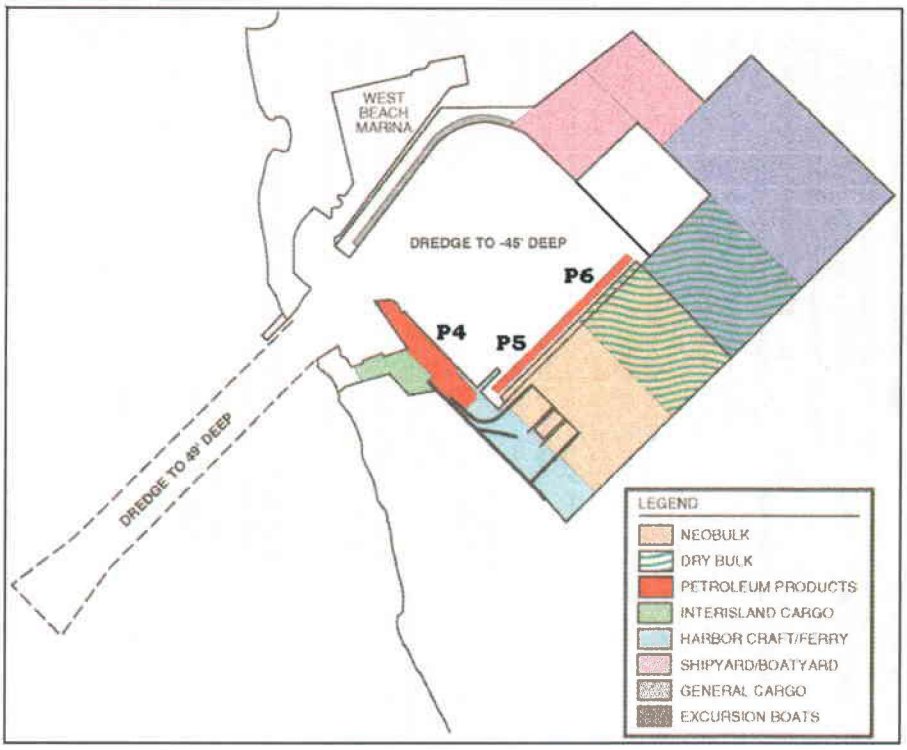

Fig. 3-3: Barbers Point Harbor Pier Locations.

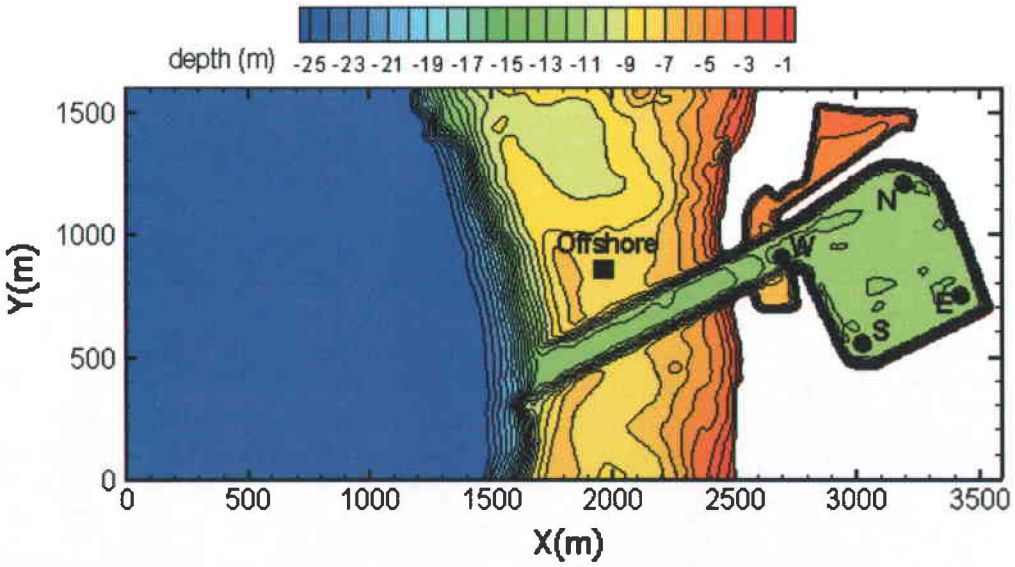

Fig. 3-4: Barbers Point Harbor Computational Domain (●,■, locations of bottom-mounted pressure sensors).

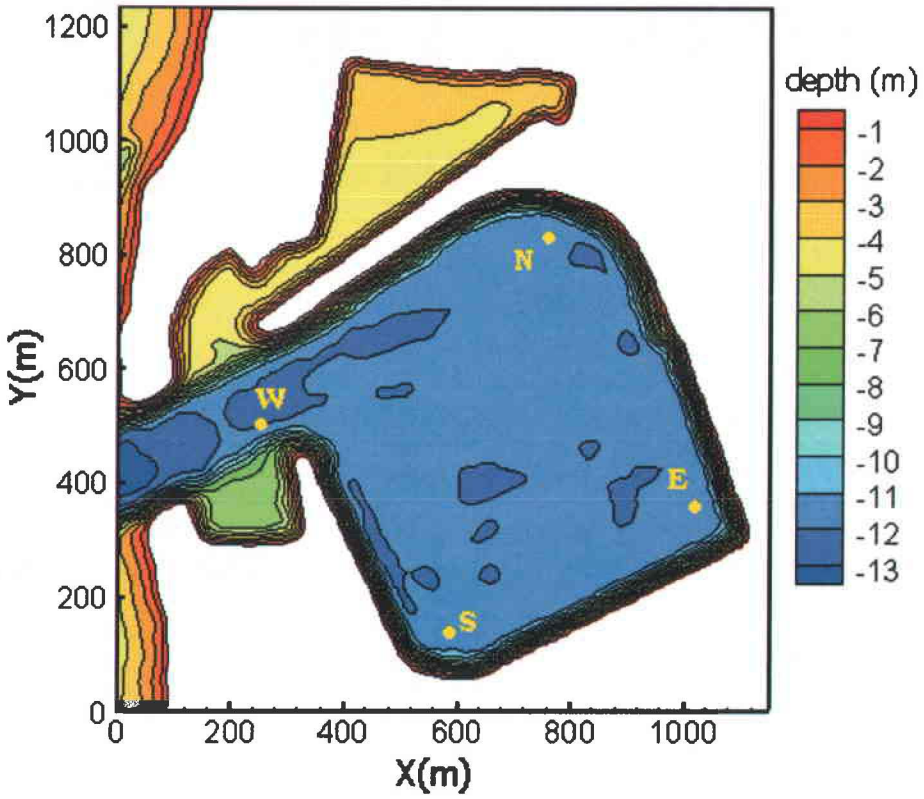

Fig. 3-5: Barbers Point Harbor Bathymetry (●, locations of bottom-mounted pressure sensors).

Fig. 3-6: Kahului Harbor Aerial View (http://www.state.hi.us).

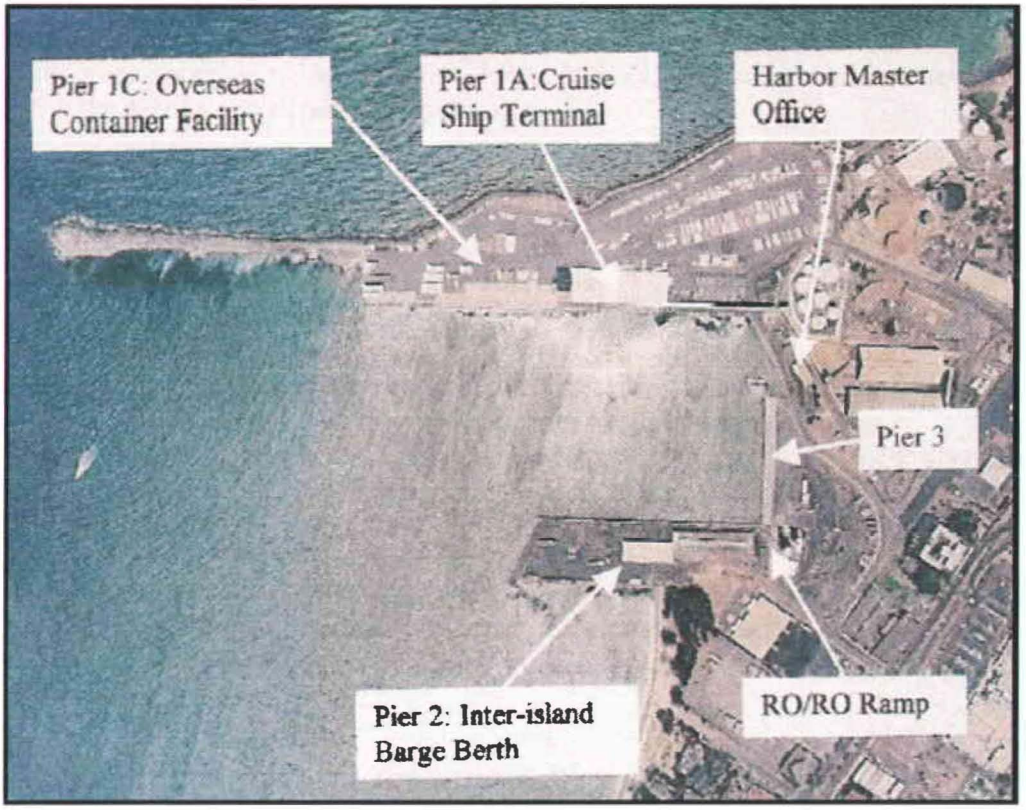

Fig. 3-7: Kahului Harbor Pier Locations (http://www.state.hi.us).

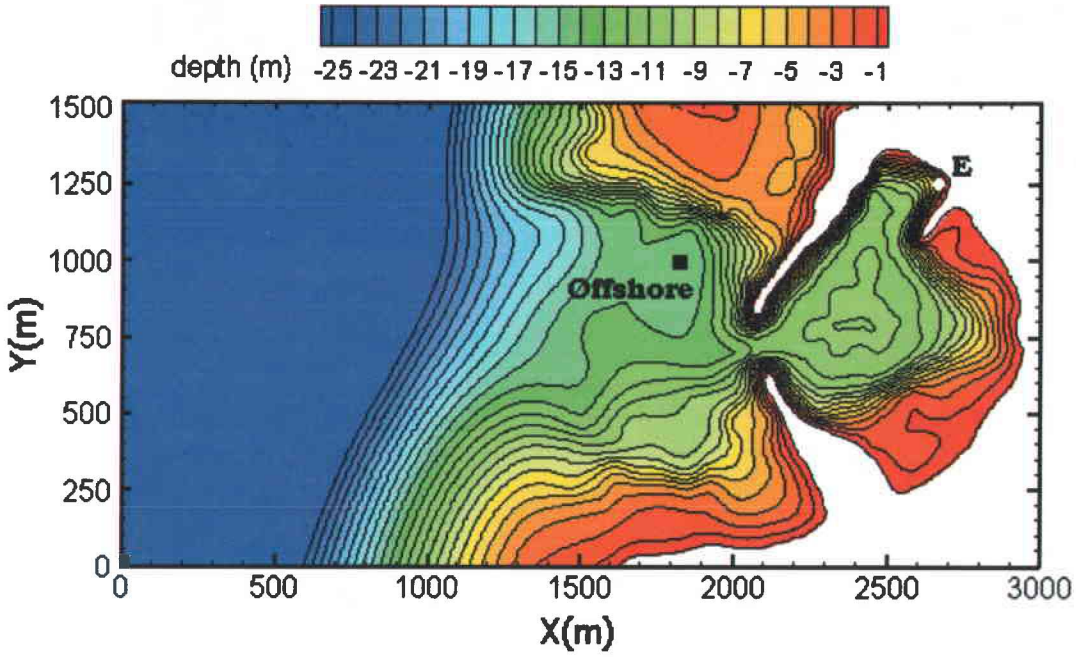

Fig. 3-8: Kahului Harbor Computational Domain (●,■, locations of bottom-mounted pressure sensors).

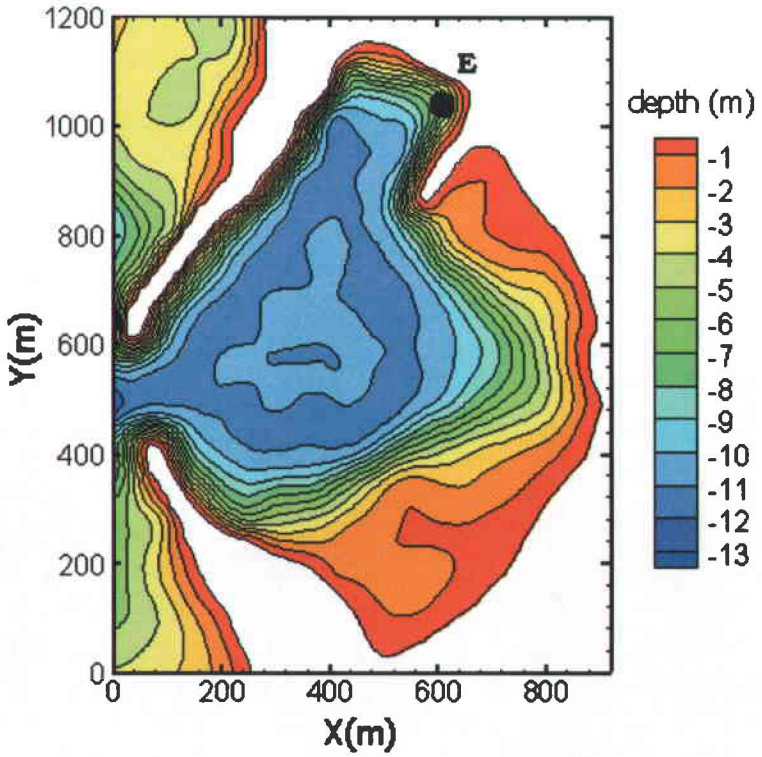

Fig. 3-9: Kahului Harbor Bathymetry (●, locations of bottom-mounted pressure sensors).

(a)

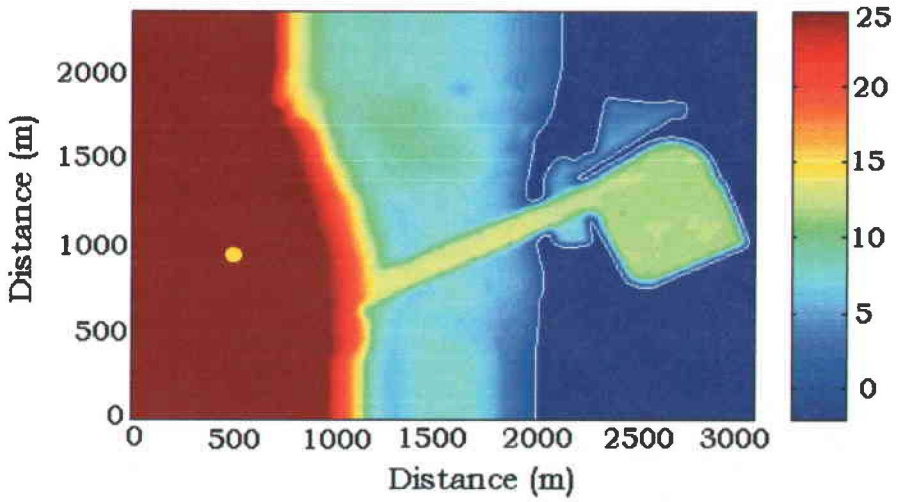

(b)

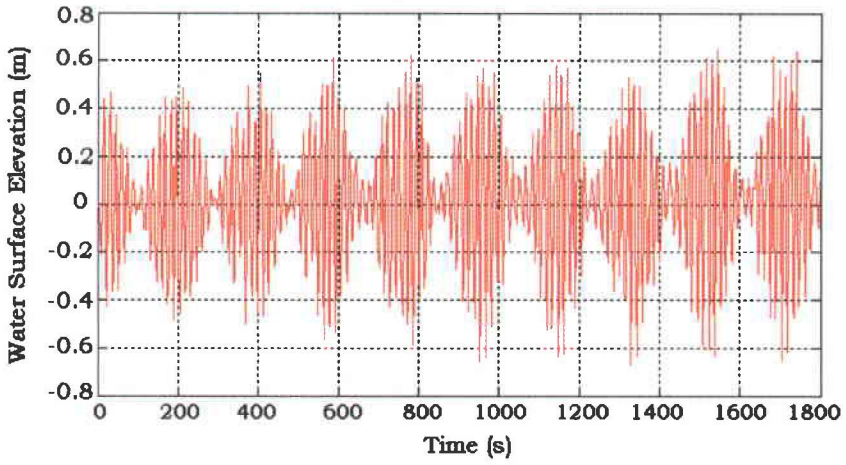

(c)

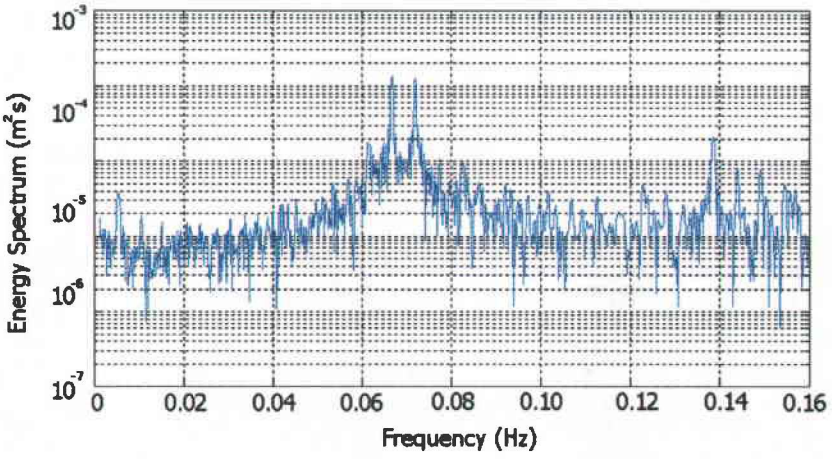

Fig. 3-10: Time Series and Amplitude Spectrum of Incident Waves. (a) Computational Domain Probe (●). (b) Time Series. (c) Resulting Normalized Wave Spectrum.

(a)

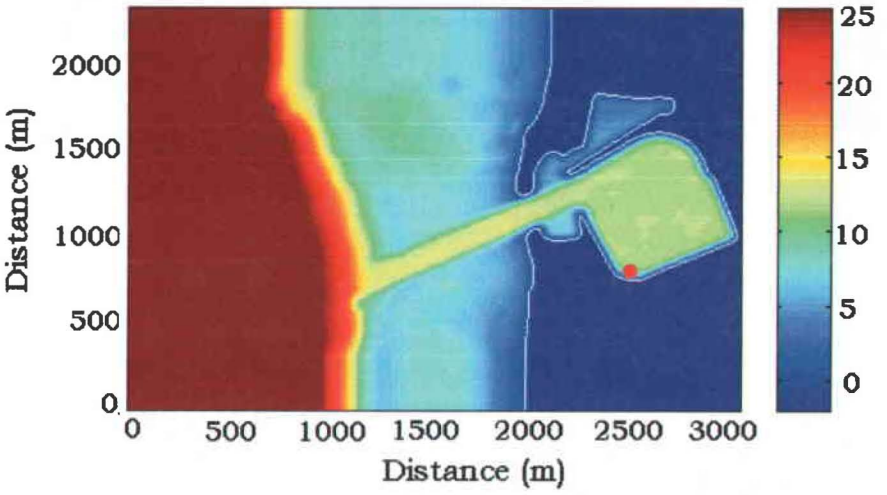

(b)

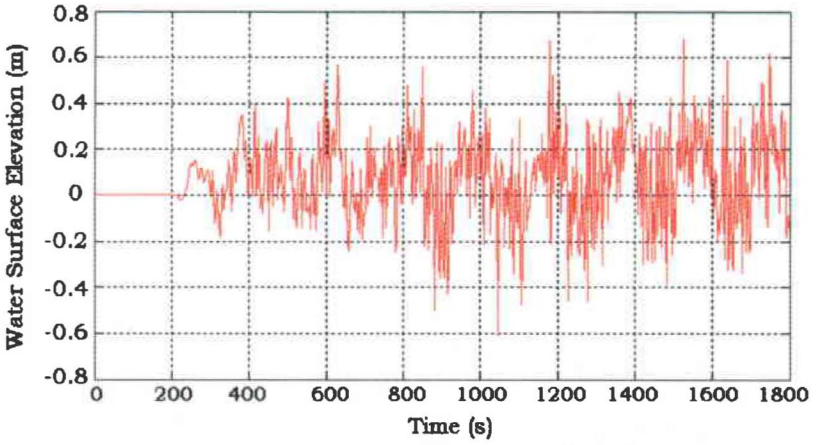

(c)

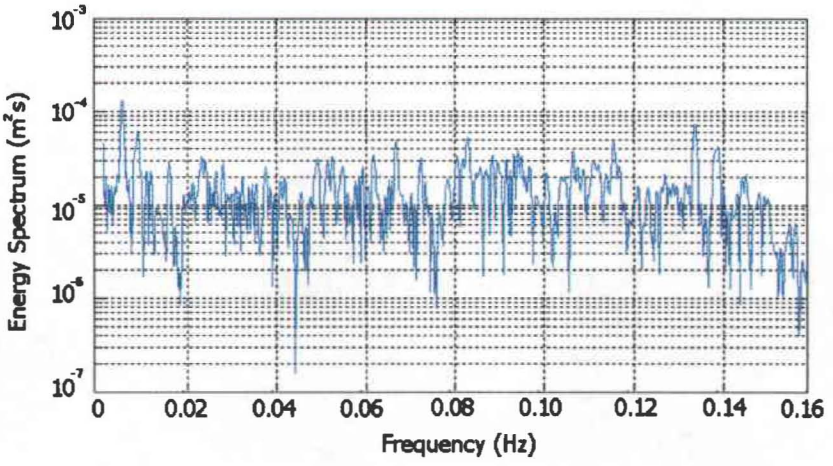

Fig. 3-11: Time Series and Amplitude Spectrum in Barbers Point Harbor (a) Computational Domain Probe (●). (b) Time Series. (c) Resulting Normalized Wave Spectrum.

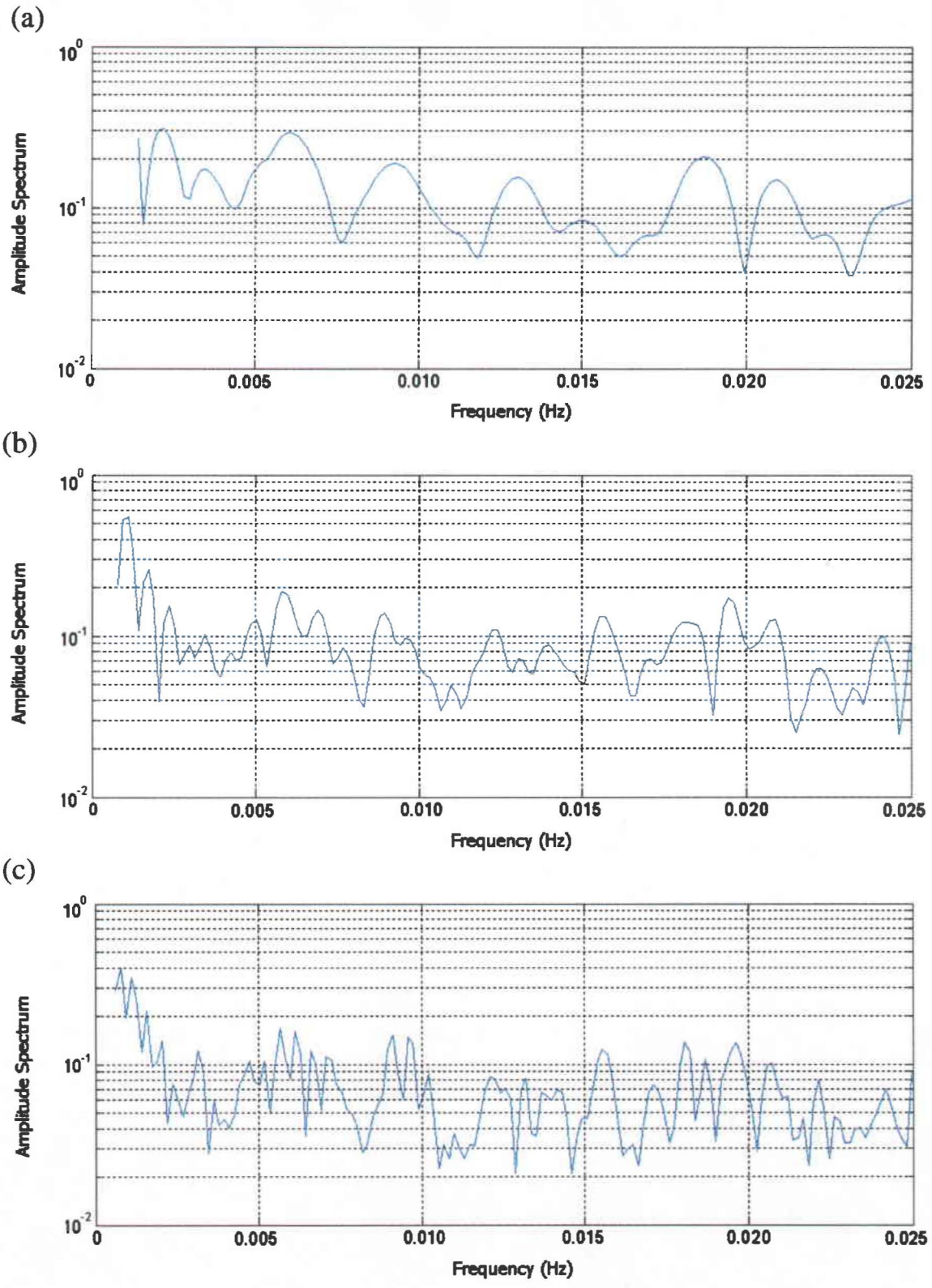

Fig. 3-12: Barbers Point Harbor Frequency Response with Varying Simulation Time. (a) 15 min. (b) 30 min. (c) 45 min.

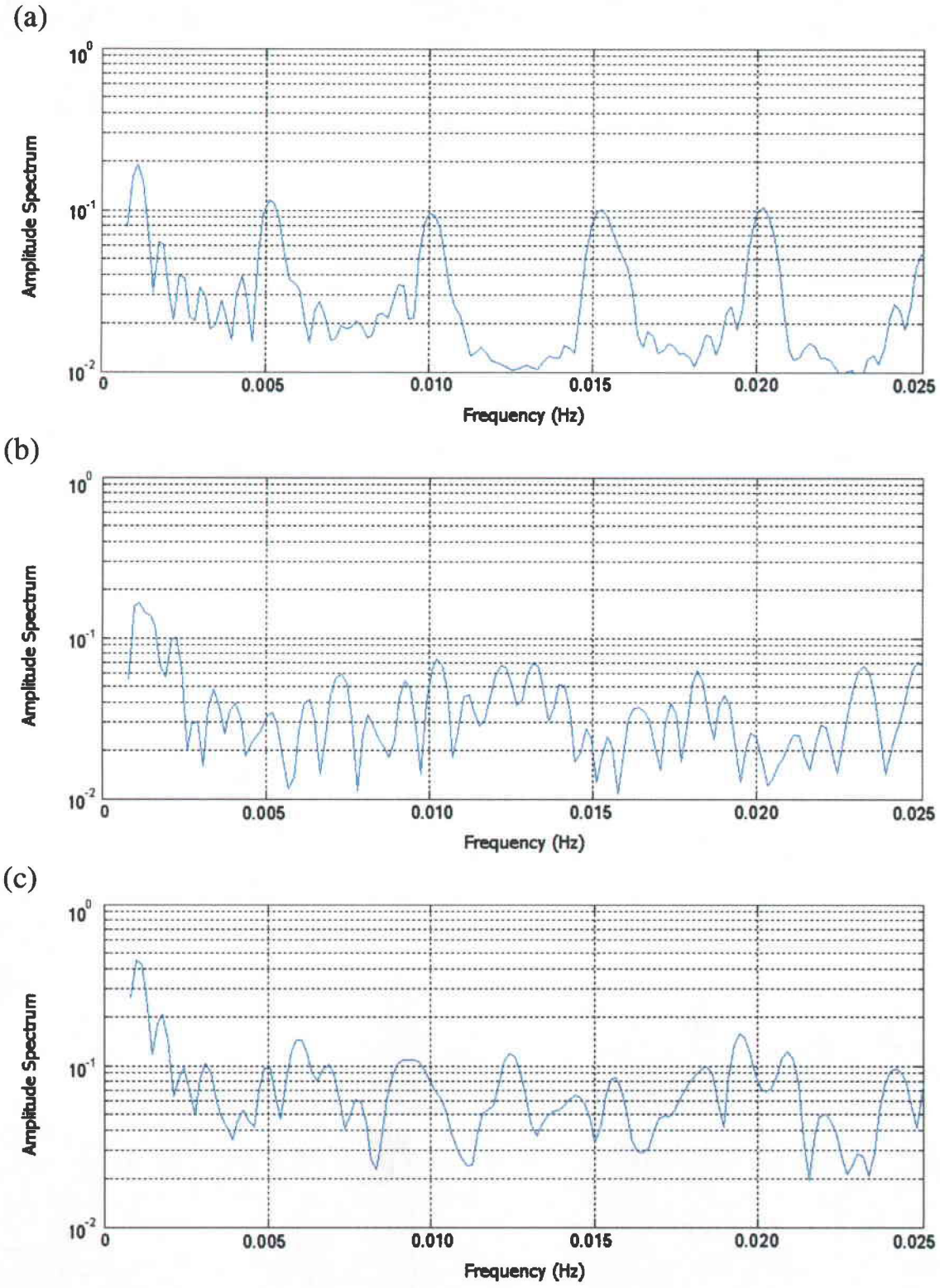

Fig. 3-13: Barbers Point Harbor Frequency Response with Varying Wave Spectrum Resolution. (a) 0.005 Hz. (b) 0.001 Hz. (c) 0.0005 Hz.

(a)

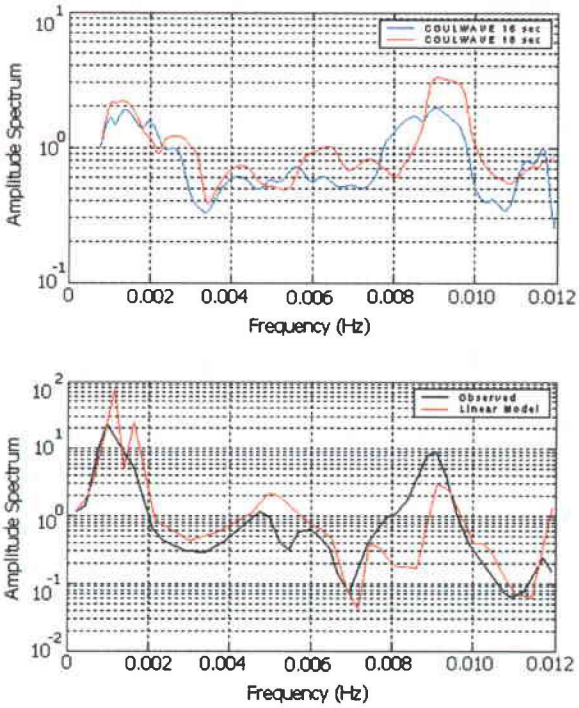

(b)

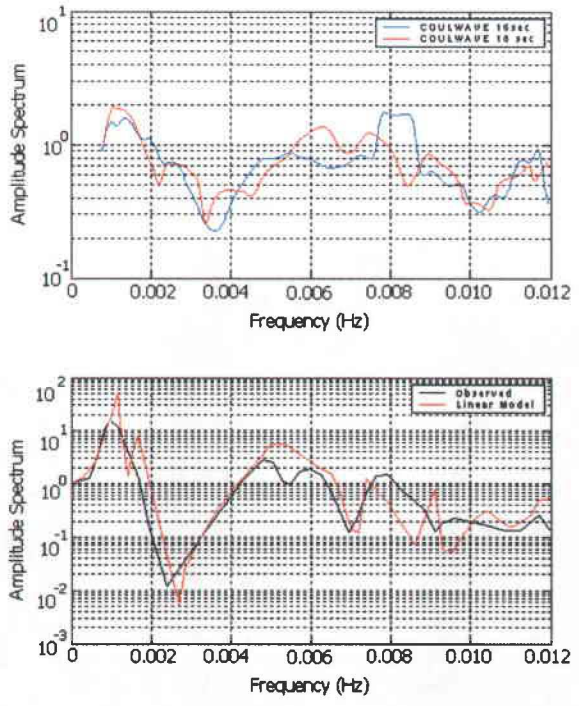

Fig. 3-14: Comparison of Computed and Measured Response Spectra in Barbers Point Harbor. (a) East. (b) West.

(c)

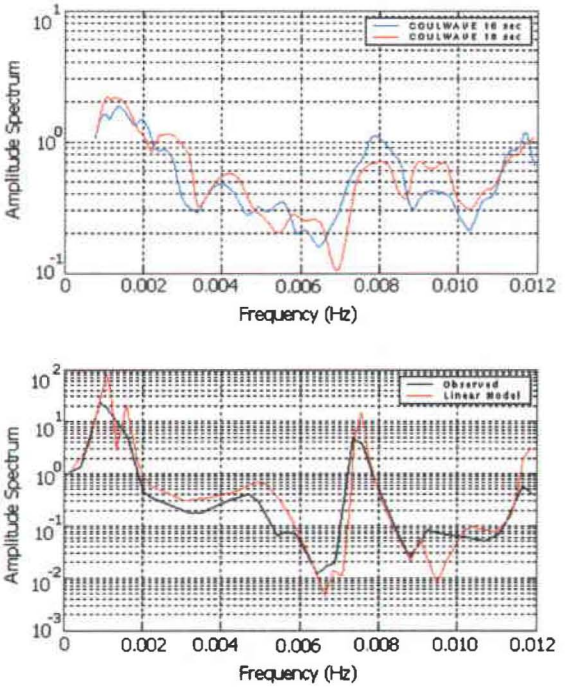

(d)

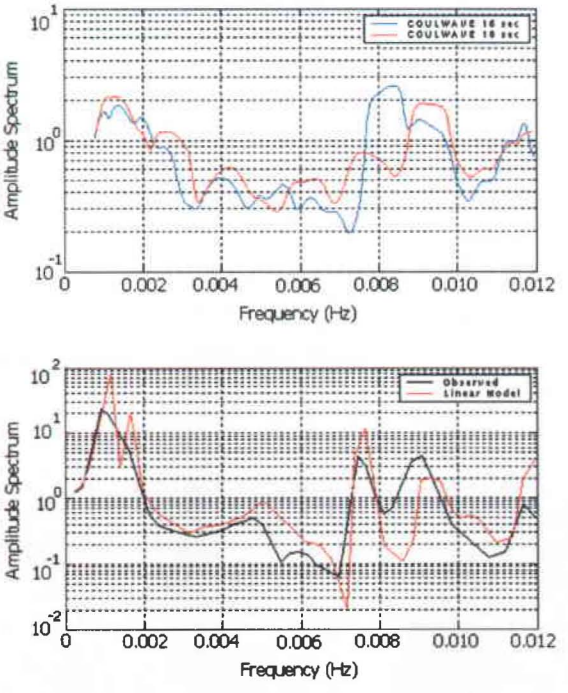

Fig. 3-14: (Cont) Comparison of Computed and Measured Response Spectra in Barbers Point Harbor. (c) North. (d) South.

(a)

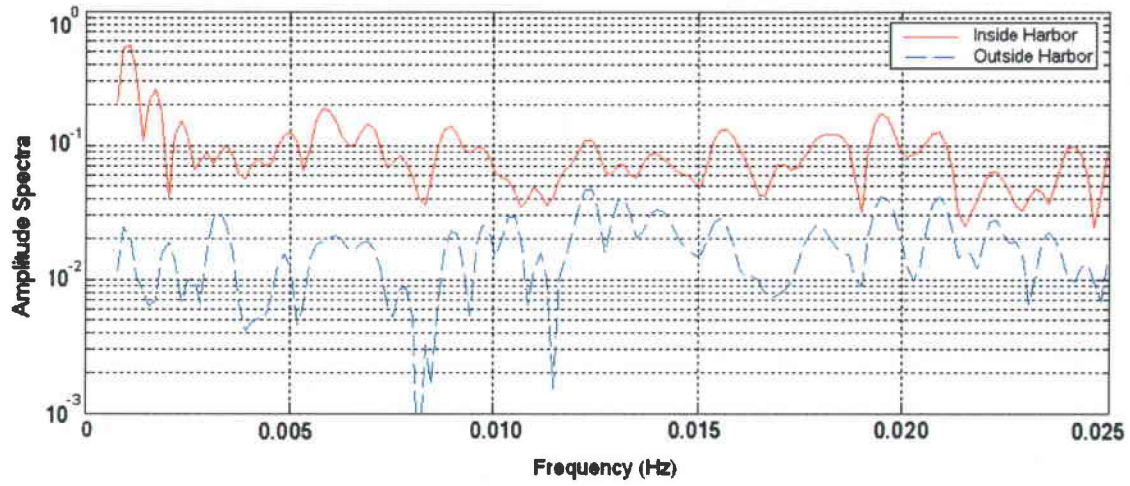

(b)

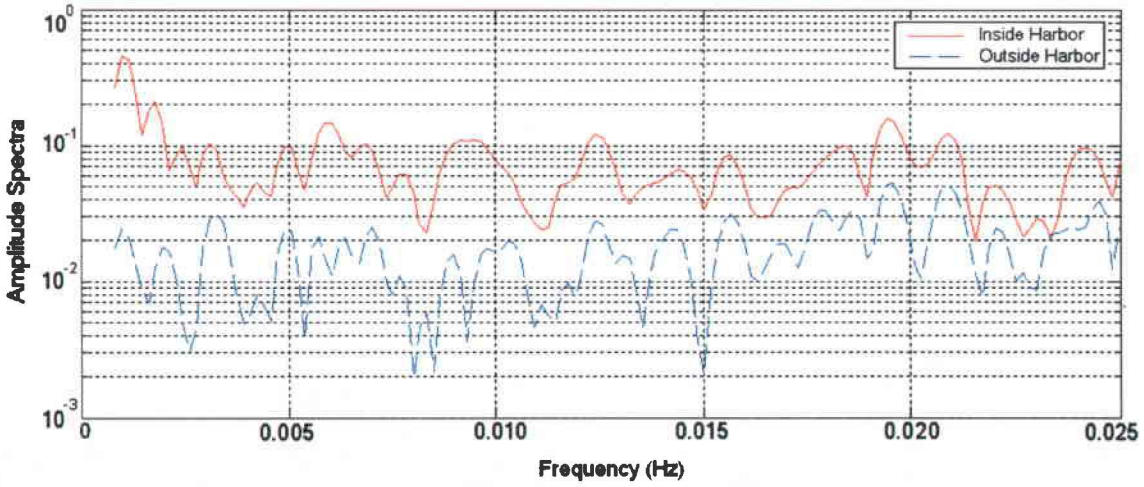

Fig. 3-15: Comparison of Amplitude Spectra Inside and Outside of Barbers Point Harbor. (a) T_p = 16 sec. (b). T_p = 18 sec.

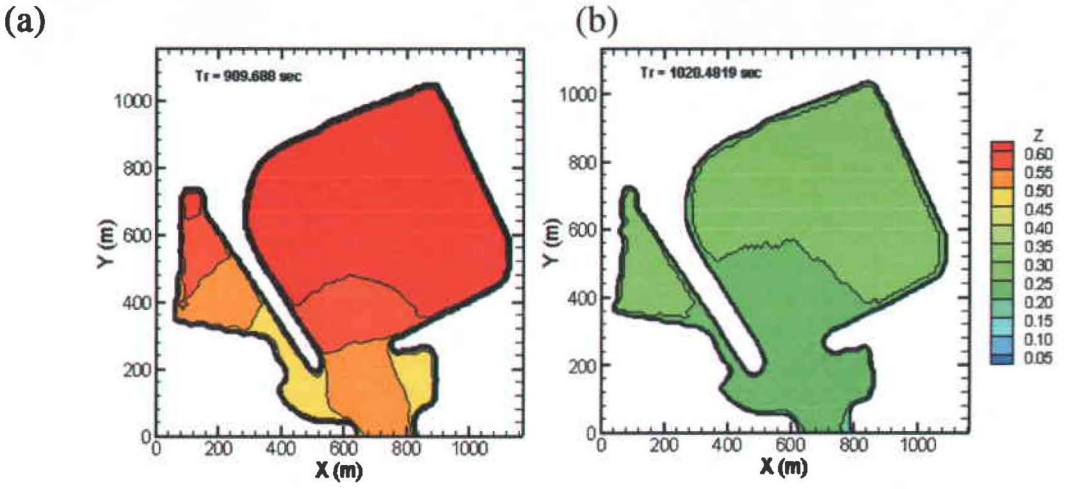

Fig. 3-16: Barbers Point Harbor Grave mode Contour Plot. (a) T_p = 16s. (b) T_p = 18s.

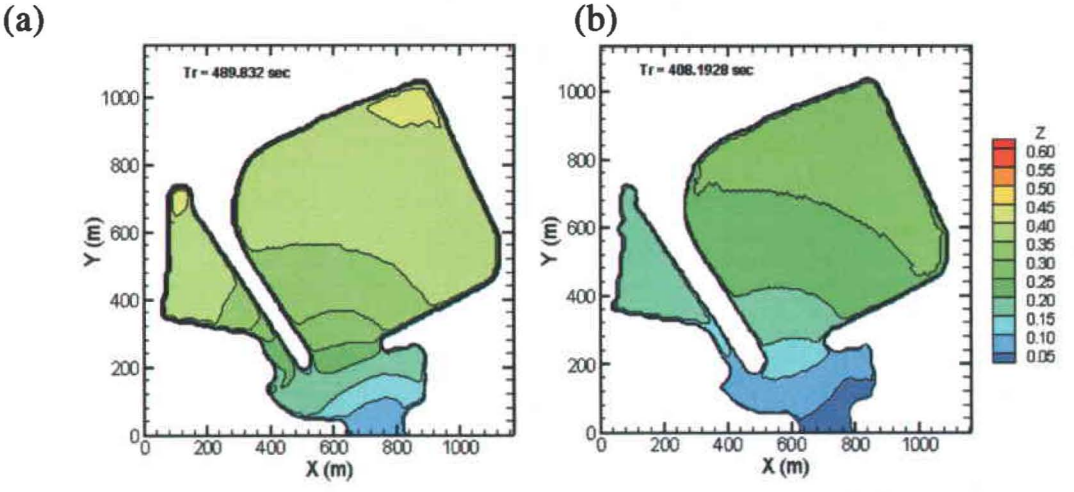

Fig. 3-17: Barbers point Harbor: 1st Mode of Oscillation. (a) T_p = 16s. (b) T_p = 18s.

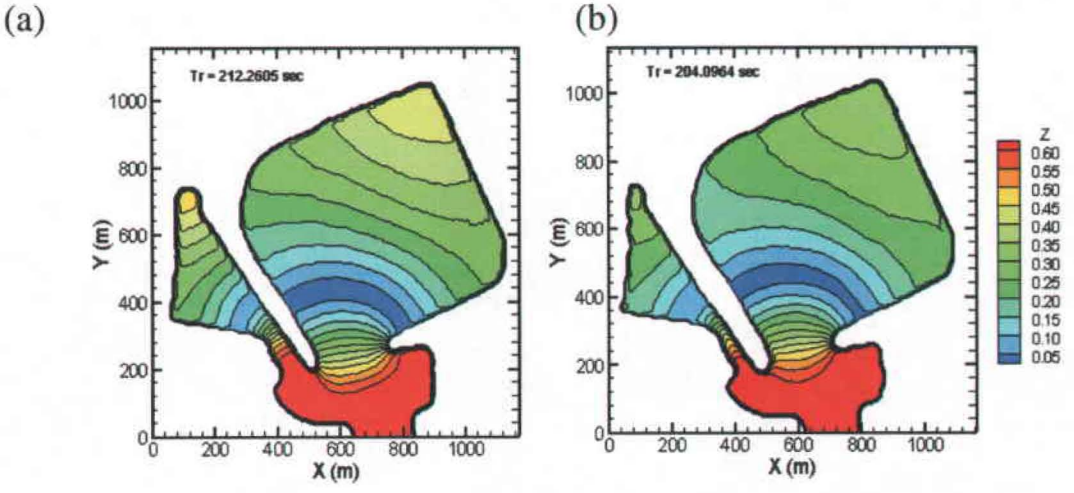

Fig. 3-18: Barbers point Harbor: 2nd Mode of Oscillation. (a) T_p = 16s. (b) T_p = 18s.

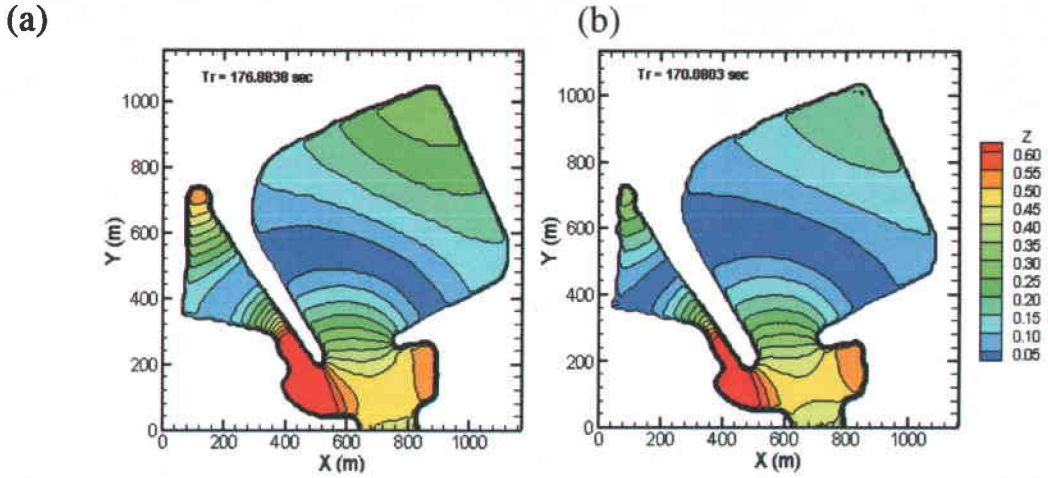

Fig. 3-19: Barbers point Harbor: Variance of 2nd Mode of oscillation. (a) T_p = 16s. (b) T_p = 18s.

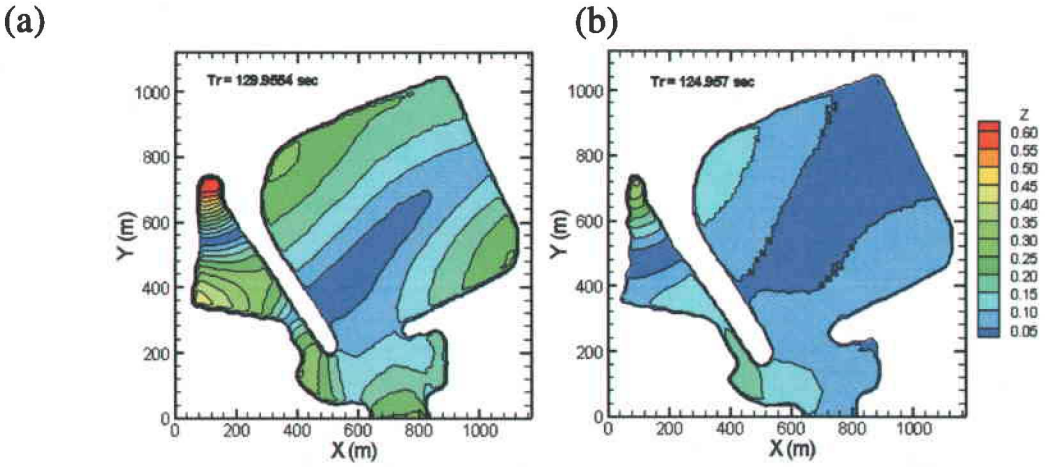

Fig. 3-20: Barbers point Harbor: 3rd Mode of Oscillation. (a) T_p = 16s. (b) T_p = 18s.

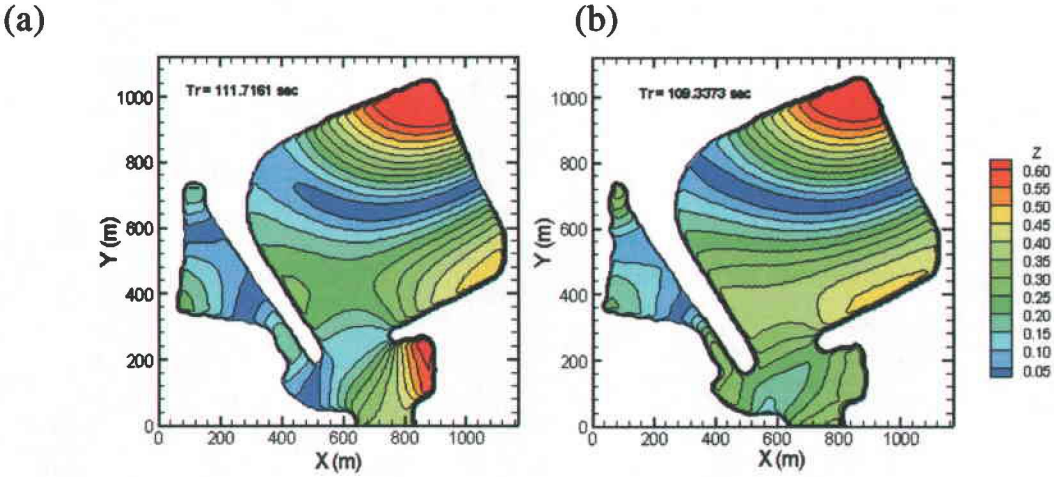

Fig. 3-21: Barbers point Harbor: 4th Mode of Oscillation. (a) T_p = 16s. (b) T_p = 18s.

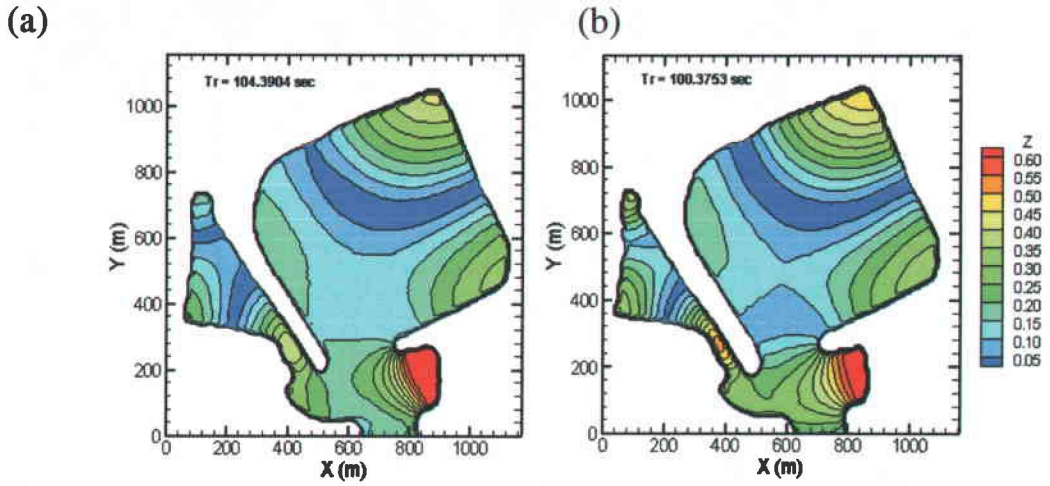

Fig. 3-22: Barbers point Harbor: Variance of 4th Mode of Oscillation. (a) T_p = 16s. (b) T_p = 18s.

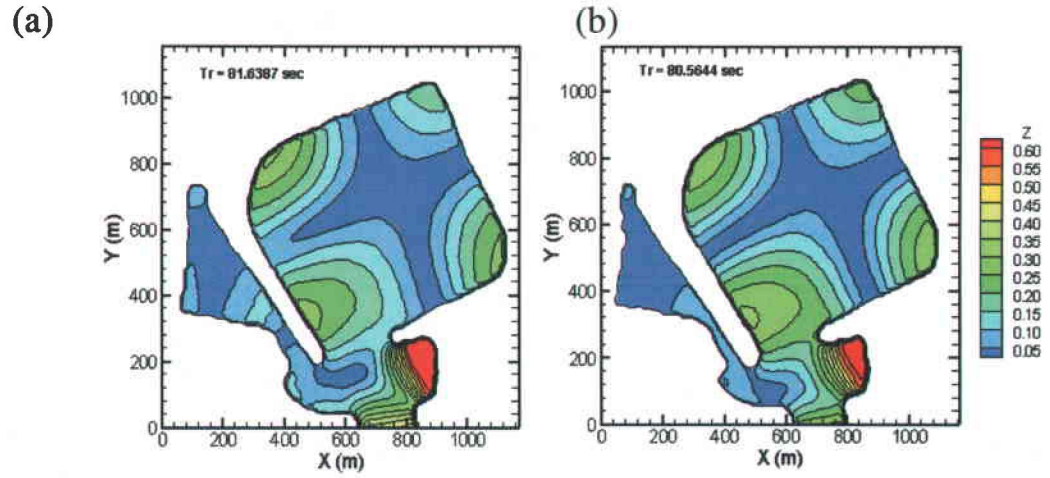

Fig. 3-23: Barbers point Harbor: 5th Mode of Oscillation. (a) T_p = 16s. (b) T_p = 18s.

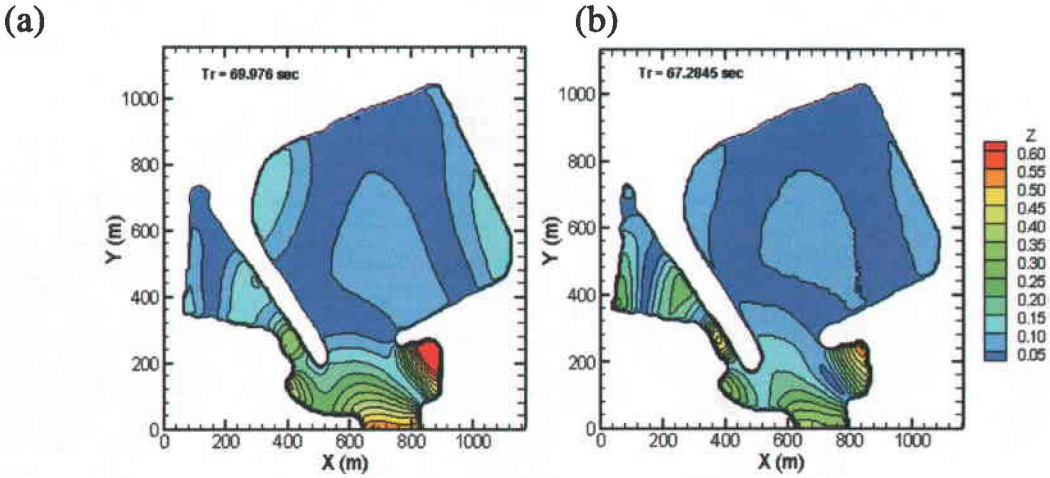

Fig. 3-24: Barbers point Harbor: 6th Mode of Oscillation. (a) T_p = 16s. (b) T_p = 18s.

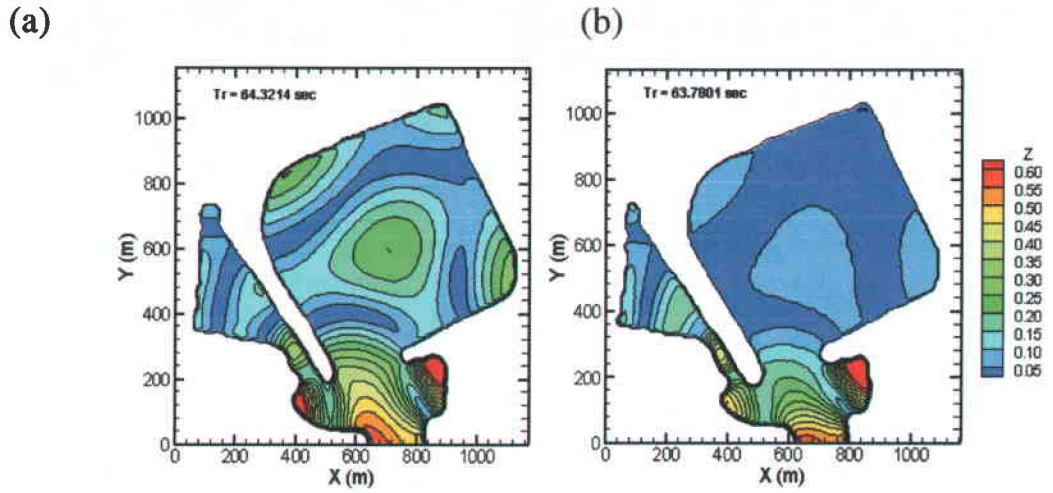

Fig. 3-25: Barbers point Harbor: 7th Mode of Oscillation. (a) T_p = 16s. (b) T_p = 18s.

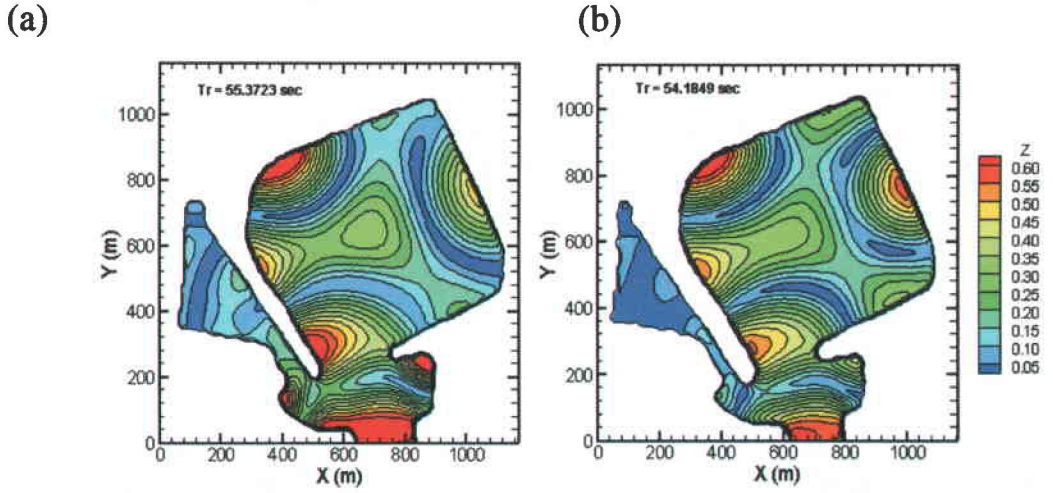

Fig. 3-26: Barbers point Harbor: 8h Mode of Oscillation. (a) T_p = 16s. (b) T_p = 18s.

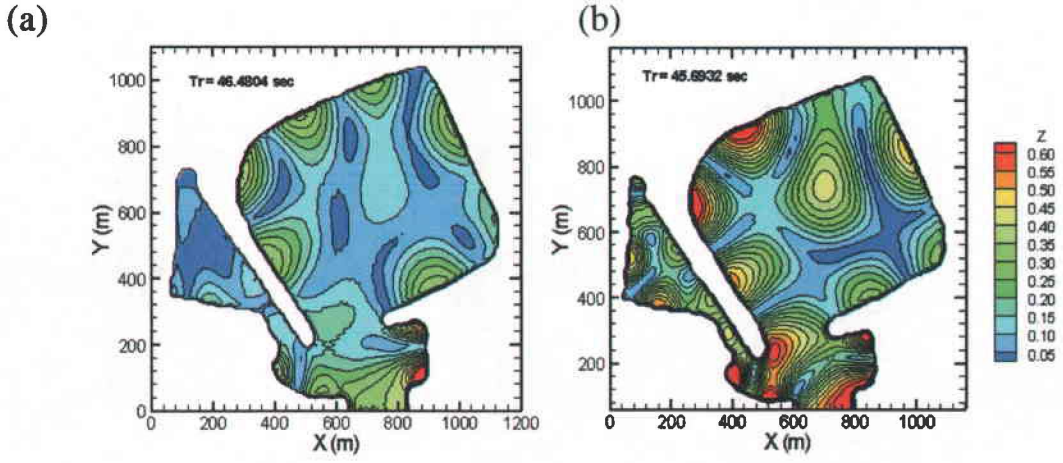

Fig. 3-27: Barbers point Harbor: 9h Mode of Oscillation. (a) T_p = 16s. (b) T_p = 18s.

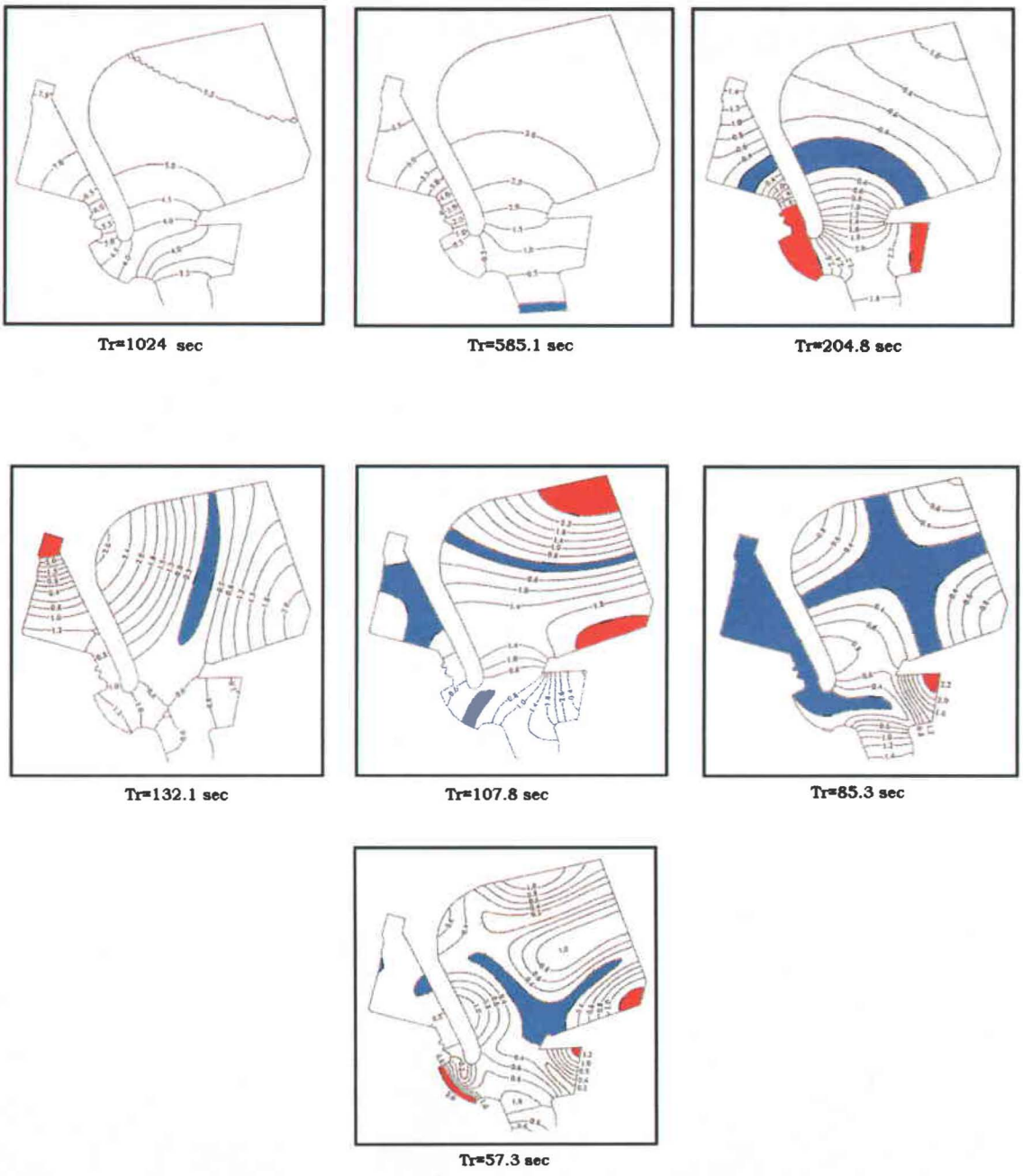

Figure 3-28: Barbers Point Harbor computed Oscillation Mode with Linear Model (Lillycrop et al., 1993).

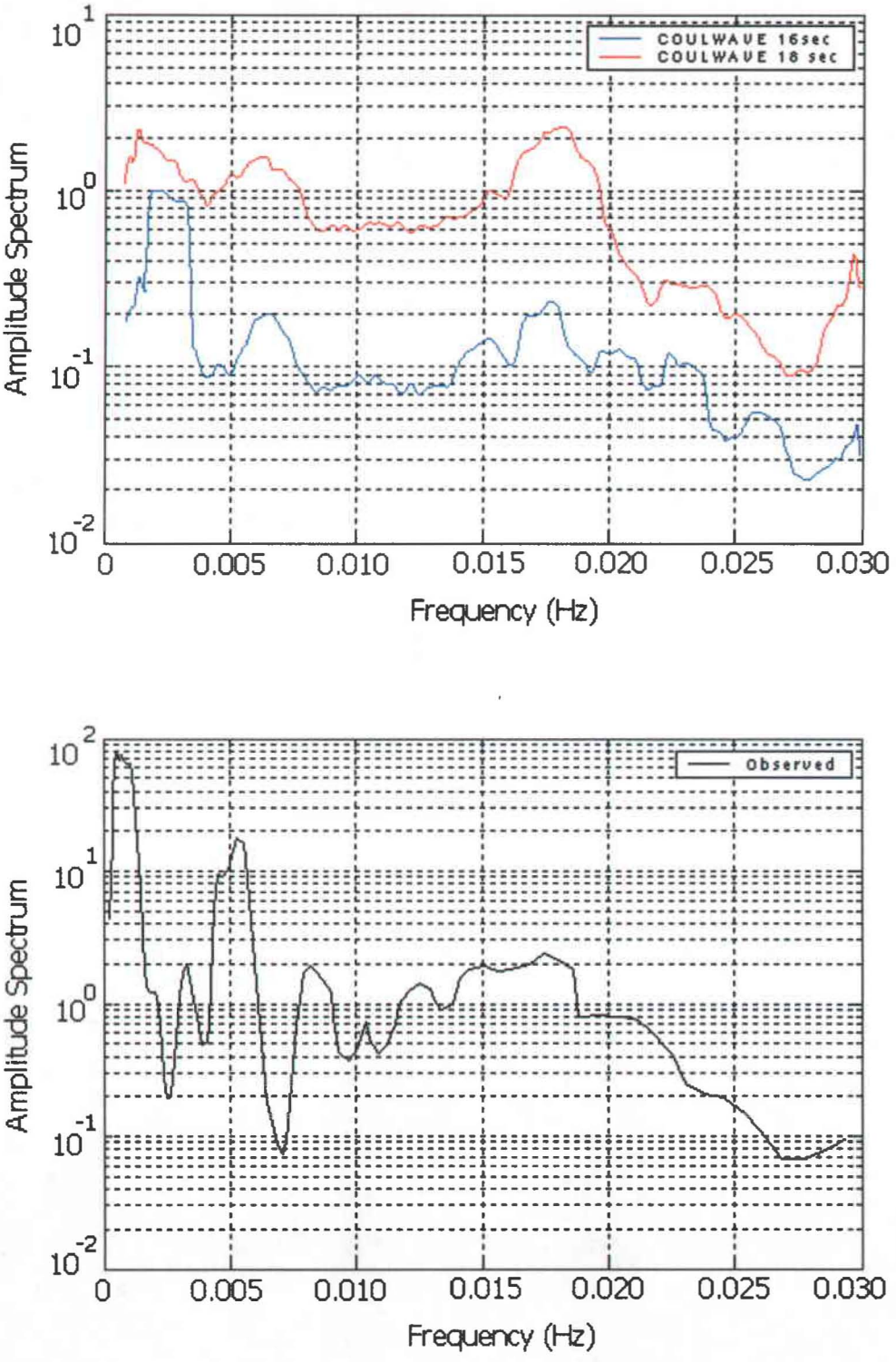

Fig. 3-29: Kahului Harbor Frequency Response Numerical and Observed Comparison Plots.

(a)

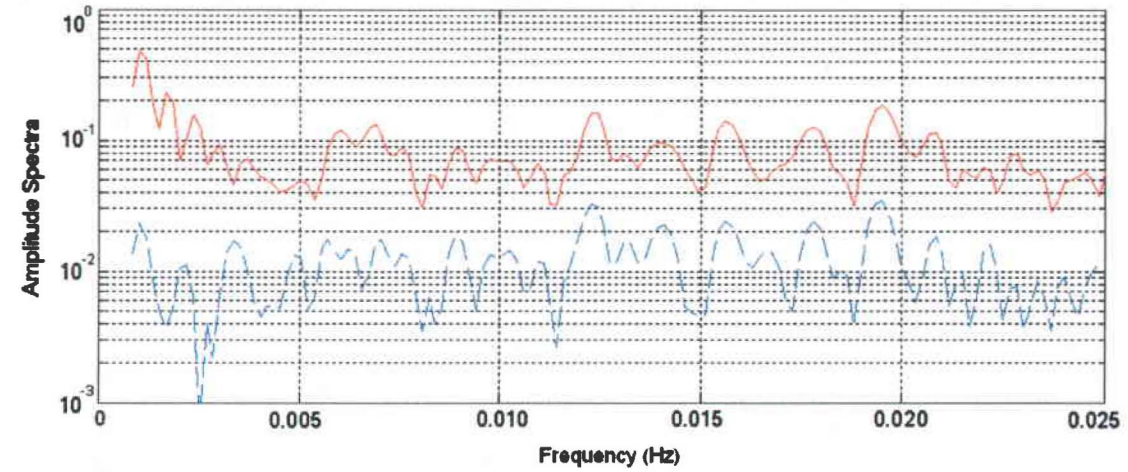

(b)

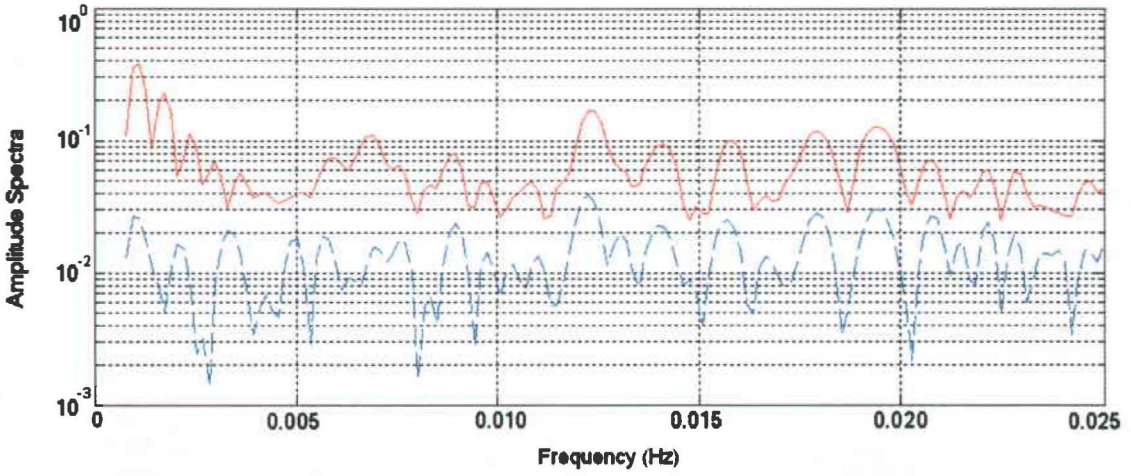

Fig. 3-30: Comparison of Amplitude Spectra Inside and Outside of Kahului Harbor. (a) T_p = 16 sec. (b). T_p = 18 sec.

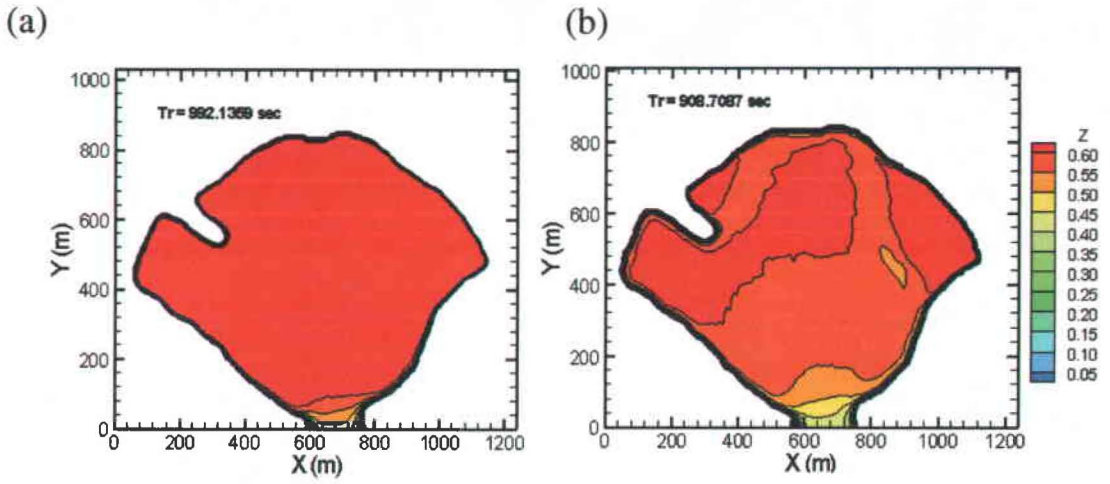

Fig. 3-31: Kahului Harbor: Grave mode Contour Plot. (a) T_p = 16s. (b) T_p = 18s.

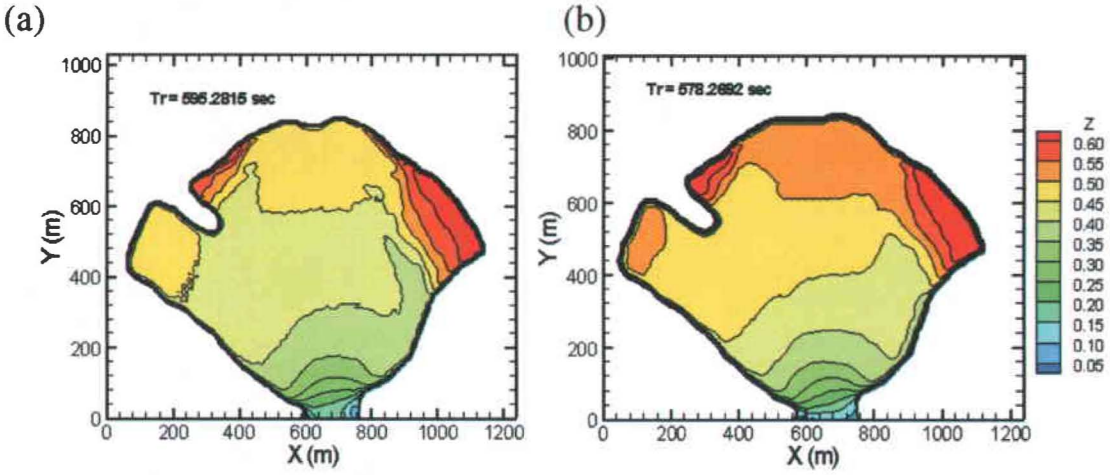

Fig. 3-32: Kahului Harbor: 1st Mode of Oscillation. (a) T_p = 16s. (b) T_p = 18s.

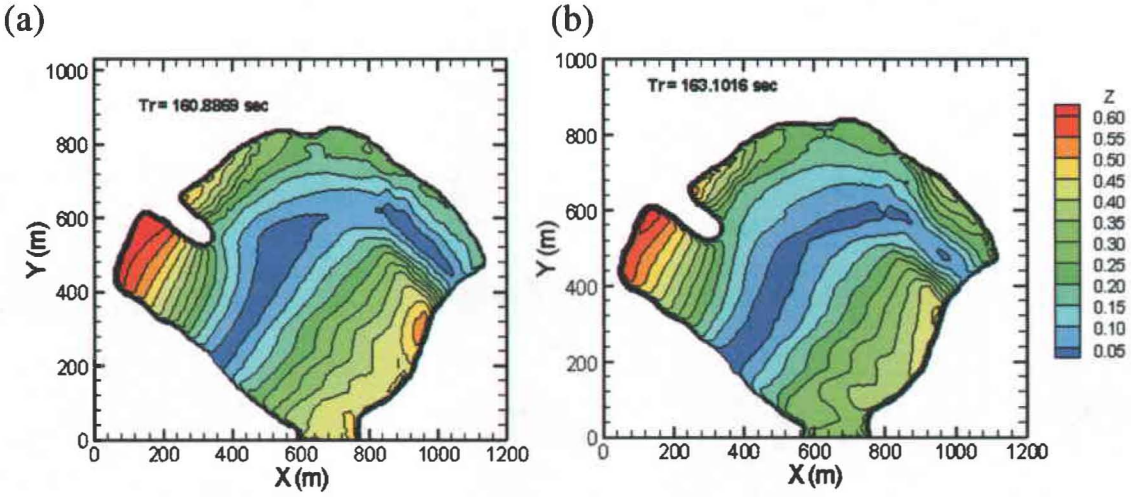

Fig. 3-33: Kahului Harbor: 2nd Mode of Oscillation. (a) T_p = 16s. (b) T_p = 18s.

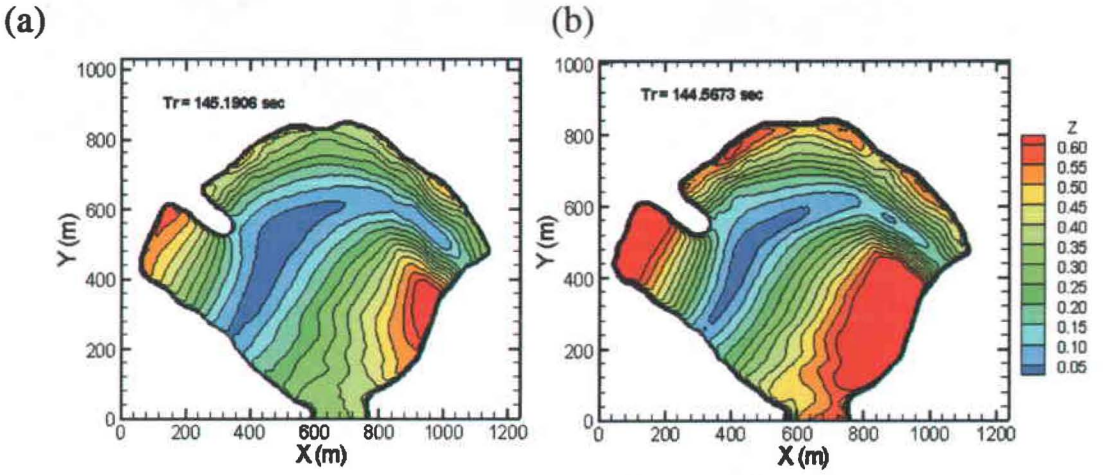

Fig. 3-34: Kahului Harbor: Variance of 2nd Mode of oscillation. (a) T_p = 16s. (b) T_p = 18s.

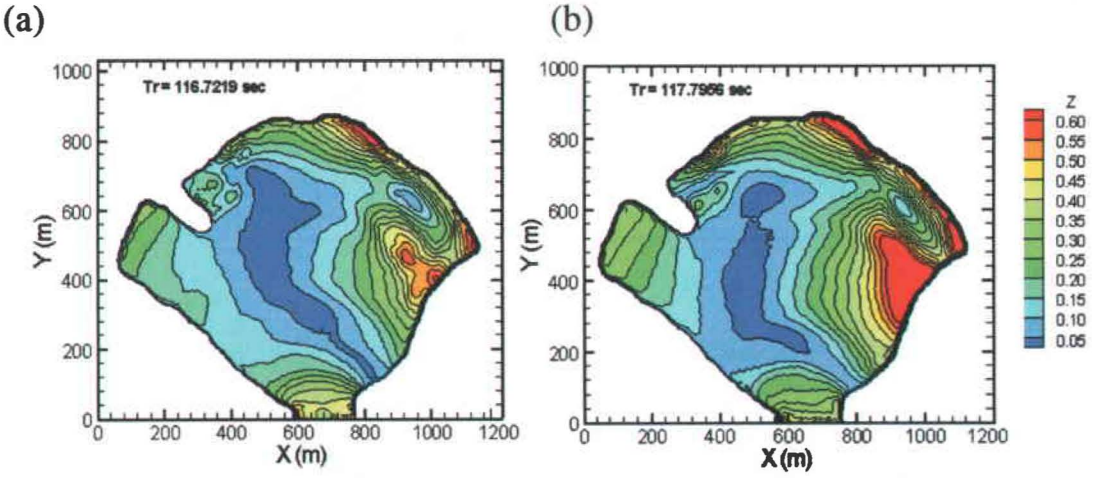

Fig. 3-35: Kahului Harbor: 3rd Mode of Oscillation. (a) T_p = 16s. (b) T_p = 18s.

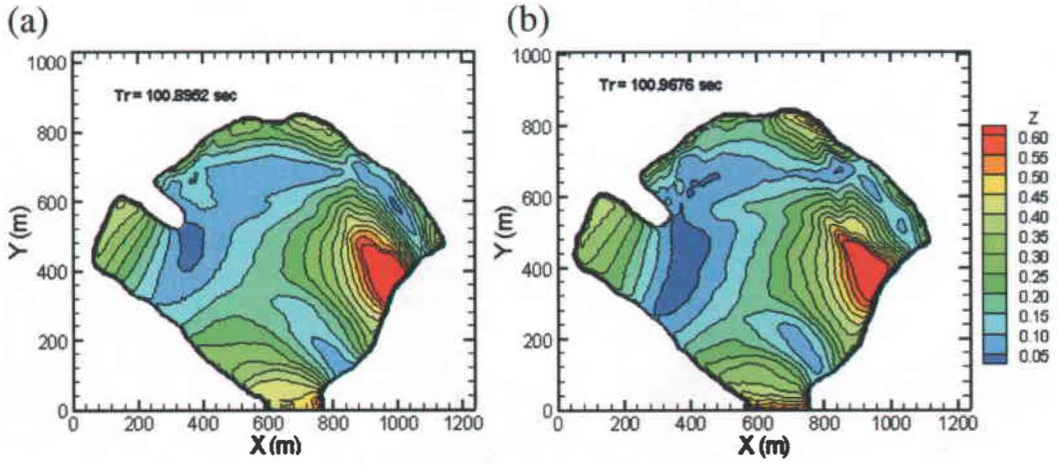

Fig. 3-36: Kahului Harbor: 4th Mode of Oscillation. (a) T_p = 16s. (b) T_p = 18s.

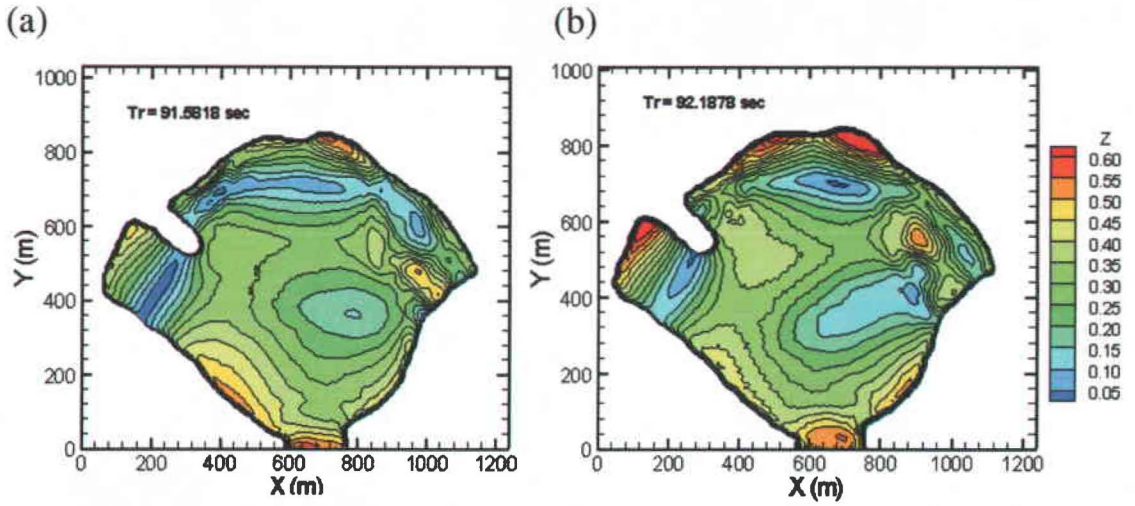

Fig. 3-37: Kahului Harbor: 5th Mode of Oscillation. (a) T_p = 16s. (b) T_p = 18s.

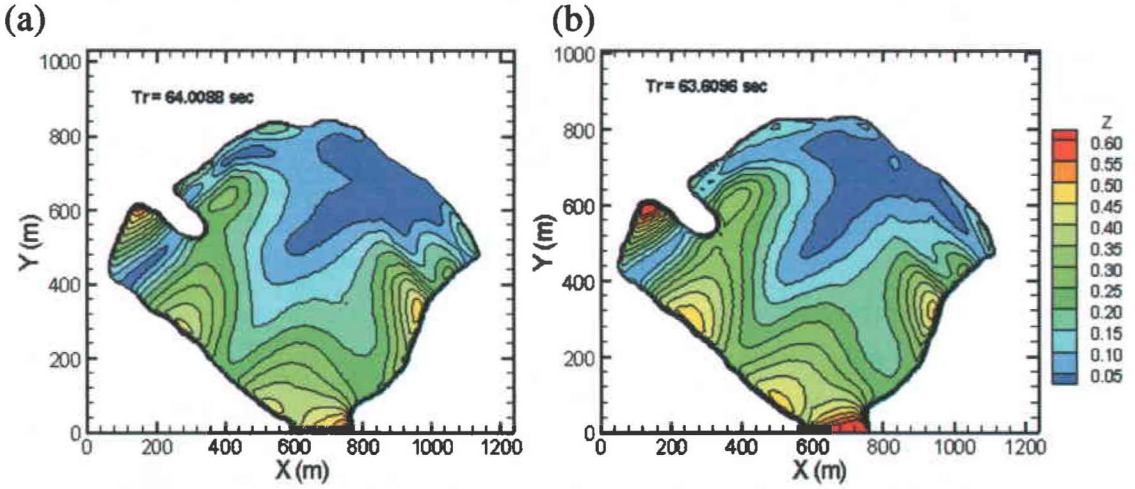

Fig. 3-38: Kahului Harbor: 6th Mode of Oscillation. (a) T_p = 16s. (b) T_p = 18s.

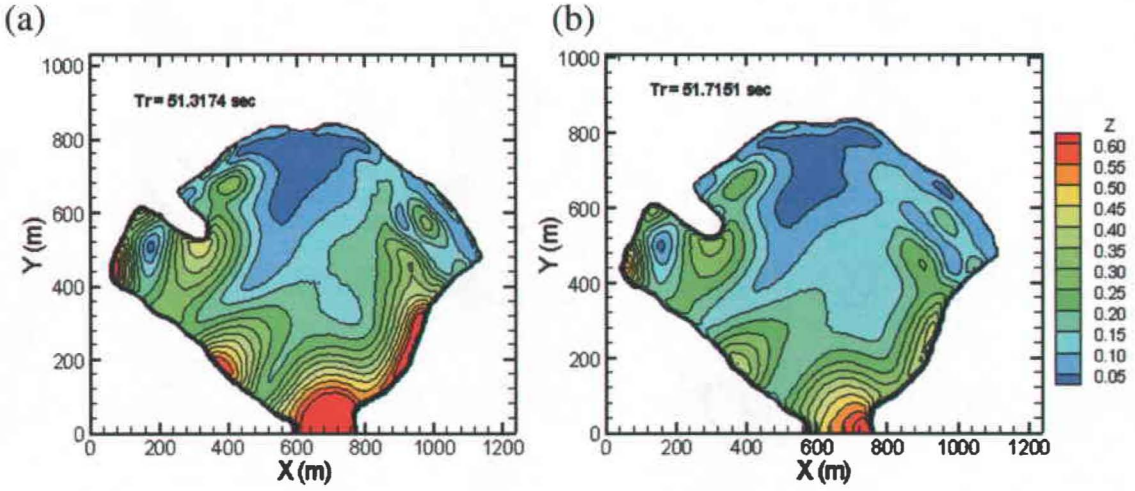

Fig. 3-39: Kahului Harbor: Variance of 6th Mode of Oscillation. (a) T_p = 16s. (b) T_p = 18s.

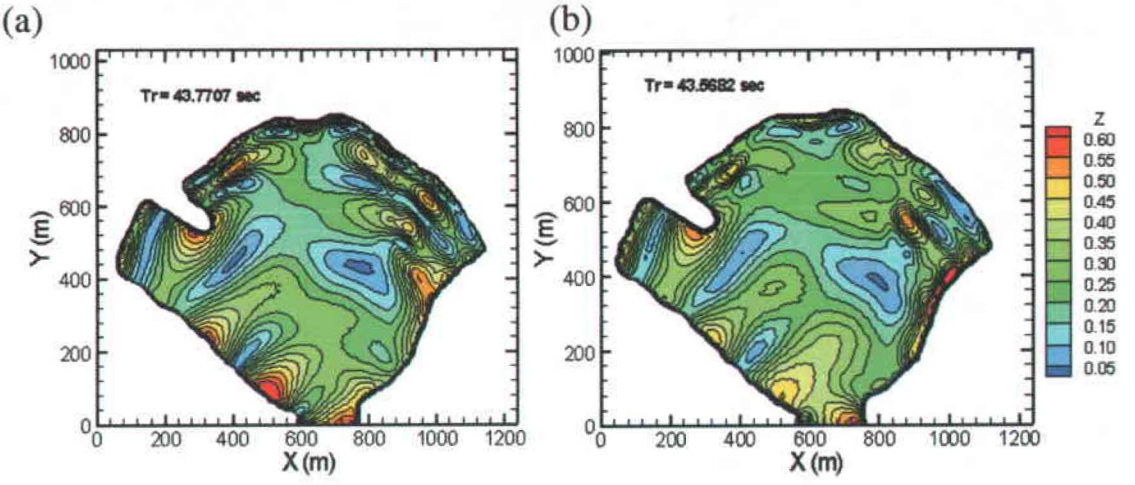

Fig. 3-40: Kahului Harbor: 7th Mode of Oscillation (a) T_p = 16s. (b) T_p = 18s.

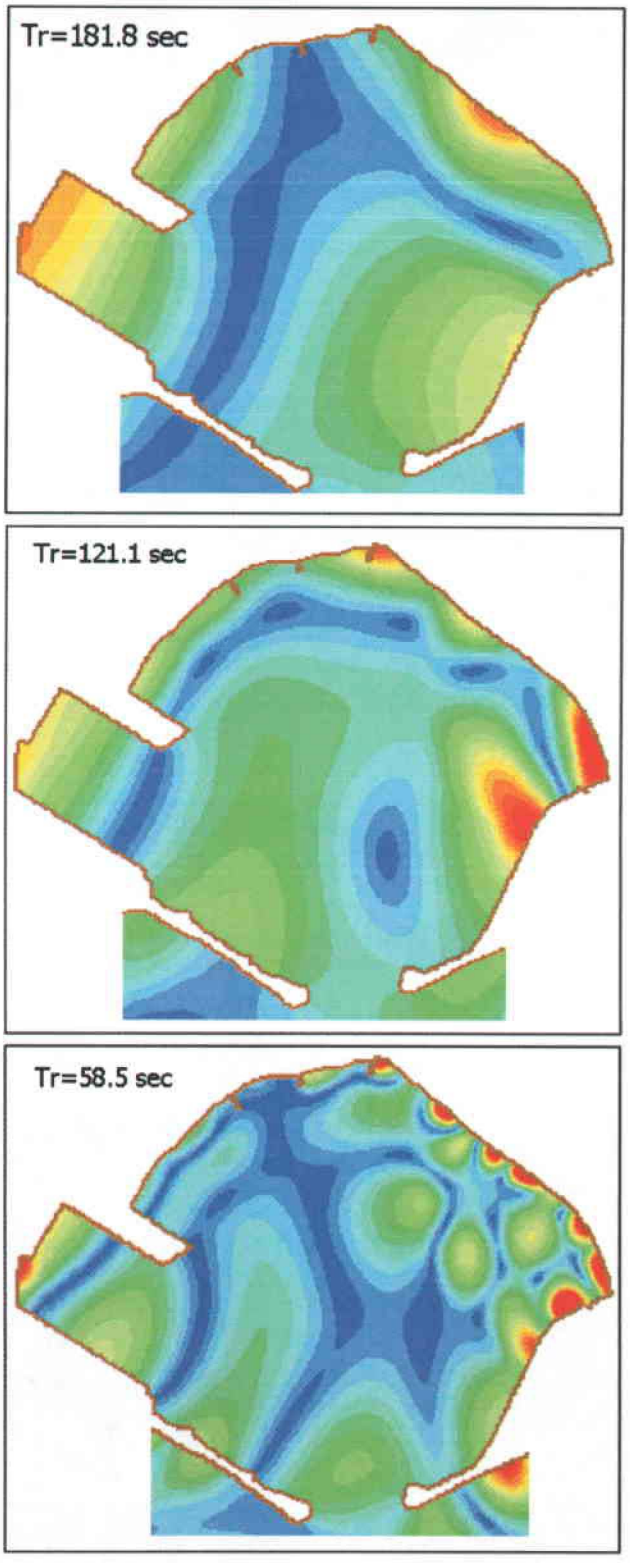

Figure 3-41: Kahului Harbor computed Oscillation Modes with the Linear Model (Thompson and Demirbilek, 2002).

LITERATURE CITED

Berkhoff, J.C.W. 1976. Mathematical models for simple harmonic linear water waves; wave refraction and diffraction. PhD thesis, Delft Technical University of Technology, Delft, The Netherlands.

Booij, N., Holthuijsen, L.H. and Ris, R.C. 1996. The SWAN wave model for shallow water. *Proceedings of the 25th International Conference on Coastal Engineering*, Orlando, Florida, Vol. 1, pp. 668-676.

Bretschneider, C.L. 1959. Wave variability and wave spectra for wind-generated gravity waves. Technical Memorandum No. 118, Beach Erosion Board, U.S. Army Corps of Engineers, Washington, D.C.

Briggs, M.J., Lillycrop, L.S., and McGehee, D.D. 1992. Comparison of Model and Field Results for Barbers Point Harbor. *Proceedings of Coastal Engineering Practice*, pp. 387-399.

Chen, Y. and Liu, P.L.-F. 1995. Modified Boussinesq equations and associated parabolic models for water wave propagation. *Journal of Fluid Mechanics*, 288, 351-381.

Chen, H.S. and Mei, C.C. 1974. Oscillations and wave forces in an offshore harbor. Report No 190, Massachusetts Institute of Technology, Cambridge, Massachusetts.

Chen, Q., Kirby, J.T., Dalrymple, R.A., Kennedy, A.B. and Chawla, A. 2000. Boussinesq modeling of wave transformation, breaking and runup, Part II: Two-dimensional. *Journal of Waterway, Port, Coastal and Ocean Engineering*, 126(1), 48-57.

Demirbilek, Z. and Panchang, V. 1998. CGWAVE: A coastal surface water wave model of the mild slope equation. Technical Report CHL-98-26, U.S. Army Engineer Waterways Experiment Station, Vicksburg, Mississippi.

Durham, D.L. 1978. Numerical analysis of harbor oscillation for Barbers Point deep-draft Harbor. Technical Report HL-78-20, U.S. Army Engineer Waterways Experiment Station, Vicksburg, Mississippi.

Hasselmann, K., Barnett, T.P., Bouws, E., Carlson, H., Cartwright, D.E., Enke, K., Ewing, J.A., Gienapp, H., Hasselmann, D.E., Kruseman, P., Meerburg, A., Muller, P., Olbers, D.J., Richter, K., Sell, W. and Walden, H. 1993. Measurements of wind-wave growth and swell decay during the Joint North Sea Wave Project (JONSWAP). *Deutschen Hydrographischen Zeitschrit*, 12(A8), 7-79.

Houston, J.R. 1981. Combined refraction and diffraction of short waves using the finite element method. *Applied Ocean Research* 3(4), 163-70.

Kennedy, A.B., Chen, Q., Kirby, J.T., and Dalrymple, R.A. 2000. Boussinesq modeling of wave transformation, breaking and runup, Part I: One-dimensional. *Journal of Waterway, Port, Coastal and Ocean Engineering*, 126(1), 39-47.

Kowalik, Z. and Bang, I. 1987. Numerical computation of tsunami runup by the upstream derivative method. *Science of Tsunami Hazards*, 5(2), 77-84.

Lee, T.T. 1985. Proposed West Beach Marina Hydraulic Model Investigation. Technical Report No. 59, James K. K. Look Laboratory of Oceanographic Engineering, University of Hawaii, Honolulu, Hawaii.

Lillycrop, L.S., Okihiro, M.S., Briggs, M.J., Harkins, G.S., and Boc, S.J. 1993. Barbers Point Harbor, Oahu, HI, Monitoring Study. MP-CERC-93-18, U.S. Army Engineer, Waterways Experiment Station, Vicksburg, Mississippi.

Liu, P.L.-F. 1994. Model equations for wave propagation from deep to shallow water. *Advances in Coastal Engineering*, 1, 125-57.

Lynett, P.J., Wu, T.R., and Liu, P.L.-F. 2002. Modeling wave runup with depth-integrated equations. *Coastal Engineering*, 46(2), 89-108.

Madsen, P.A., Murray, R. and Sorensen, O.R. 1991 A new form of the Boussinesq equations with improved linear dispersion characteristics. *Coastal Engineering*, 15, 371-388.

Nwogu, O. 1993. Alternative form of Boussinesq equations for nearshore wave propagation. *Journal of Waterway, Port, Coastal, and Ocean Engineering*, 119(6), 618-639.

Nwogu, O. 1996. Numerical prediction of breaking waves and currents with a Boussinesq model. *Proceedings of the 25th International Conference on Coastal Engineering*, Kobe, Japan, Volume 1, pp. 467-481.

Nwogu, O. and Demirbilek, Z., 2001. BOUSS-2D: A Boussinesq Wave Model for Coastal Regions and Harbors. Theoretical Background and User's Manual Report 1, U.S. Army Engineer, Waterways Experiment Station, Vicksburg, Mississippi.

Okihiro, M.S., Guza, R.T., and Seymour, R.J. 1993. Excitation of seiche in a small harbor. *Journal of Geophysical Research*, 98, 18,201-18,211.

Okihiro, M.S. and Guza, R.T. 1996. Observations of seiche forcing and amplification in three small harbors. *Journal of Waterway, Port, Coastal, and Ocean Engineering*, 122(5), 232-238.

Palmer, R.Q. 1970. Study of Proposed Barbers Point Harbor, Hawaii; Hydraulic Model Investigation. Technical Report No. 8, US Army Engineer District, Honolulu, Hawaii.

Peregrine, D.H. 1967. Long waves on a beach. *Journal of Fluid Mechanics*, 27, 815-827.

Pierson, W. J. and Moskowitz, L., 1964. A proposed spectral from for fully developed wind seas based on the similarity theory of S. A. Kitaigorodskii. *Journal of Geophysical Resources*, 69(24), 5181-5203.

Sand, S.E. 1982. Long wave problems in laboratory models. *Journal of Waterway, Port, Coastal, and Ocean Engineering*, 108(4), 492-503

Sorensen, R.M. and Seelig, W.N. 1986. Hydraulics of Great Lakes inlet-harbor systems. *Proceedings of the 15th Conference on Coastal Engineering*, Honolulu, Hawaii.

St. Denis, M. and Pierson, W. 1953. On the motions of ships in confused seas. *Transactions of the Society of Naval Architects and Marine Engineers*, 61, 280-357.

Thompson, E.F. and Demirbilek, Z. 2002. Wave Climate and Wave Response, 2025 Plan, Kahului Harbor, Maui, Hawaii. Coastal and Hydraulics Laboratory, Fort Sharter, Honolulu, Hawaii.

Tolman, H. L., 1989. The Numerical Model WAVEWATCH: A Third Generation Model for the Hindcasting of Wind Waves on Tides in Shelf Seas. Report No. 89-2, Communications on Hydraulic and Geotechnical Engineering, Delft University of Technology, Delft, The Netherlands.

WAMDI (Hasselmann, S., Hasselmann, K., Bauer, E., Janssen, P.A.E.M., Komen, G.J., Bertotti, L., Lionello, P., Guillaume, A., Cardone, V.C., Greenwood, J.A., Reistad, M., Zambresky, L. and Ewing, J.A.) 1988. The WAM model – a third generation ocean wave prediction model. *Journal of Geophysical Research*, 18(12), 1775-1810.

Wei, G. Kirby, J.T., Grilli, S.T., and Subramanya, R., 1995. A fully nonlinear Boussinesq model for surface waves. Part I. Highly nonlinear unsteady waves. *Journal of Fluid Mechanics*, 294, 71-92.

Wu, J.-K. and Liu, P.L.-F. 1990. Harbor oscillations by incident wave groups. *Journal of Fluid Mechanics*, 217, 595-613.

Xu, B. and Panchang V.G, 1993. Outgoing boundary conditions for elliptic water wave models. *Proceedings of the Royal Society of London*, Series A, 441, 575-588.

Zelt, J.A. 1991. The runup of nonbreaking and breaking solitary waves. *Coastal Engineering* 15 (3), 205-246.